

An MHD Gadget for cosmological simulations

K. Dolag^{1*}, F. Stasyszyn^{1, 2}

¹ *Max-Planck-Institut für Astrophysik, Garching, Germany*

² *Instituto de Astronomía Teórica y Experimental IATE (UNC-CONICET), Observatorio Astronómico Córdoba, Francisco N. Laprida 922, Córdoba, Argentina*

Accepted ???. Received ???; in original form ???

ABSTRACT

Various observations have showed that the hot atmospheres of galaxy clusters are magnetized. However, our understanding of the origin of these magnetic fields, their implications on structure formation and their interplay with the dynamics of the cluster atmosphere, especially in the centers of galaxy clusters is still very limited. In preparation to the upcoming new generation of radio telescopes (like EVLA, LWA, LOFAR and SKA), a huge effort is being made to learn more about cosmological magnetic fields from the observational perspective. Here we present the implementation of magneto hydrodynamics in the cosmological SPH code GADGET (Springel et al. 2001; Springel 2005). We discuss the details of the implementation and various schemes to suppress numerical instabilities as well as regularization schemes, in the context of cosmological simulations. The performance of the SPH MHD code is demonstrated in various one and two dimensional test problems, which we performed in a fully, three dimensional setup to test the code under realistic circumstances. Comparing with solutions obtained with ATHENA (Stone et al. 2008), we find excellent agreement with our SPH MHD implementation. Finally we apply our SPH MHD implementation to forming galaxy clusters within a large, cosmological box. Performing a resolution study we demonstrate the robustness of the predicted shape of the magnetic field profiles in galaxy clusters, which is in good agreement with previous studies.

Key words: (magnetohydrodynamics)MHD - magnetic fields - methods: numerical - galaxies: clusters

1 INTRODUCTION

Magnetic fields have been detected in galaxy clusters by radio observations, so far via the Faraday Rotation Signal of the magnetized cluster atmosphere towards polarized radio sources in or behind clusters (see Carilli & Taylor 2002; Govoni & Feretti 2004, for recent reviews) and from diffuse synchrotron emission of the cluster atmosphere (see Govoni & Feretti 2004; Ferrari et al. 2008, for recent reviews). However, our understanding of their origin, their implications on structure formation and their interplay with the dynamics of the cluster atmosphere, especially in the centers of clusters is still very limited.

In preparation to the upcoming new generation of radio telescopes (like EVLA, LWA, LOFAR and SKA), a huge effort is being made to learn more about cosmological magnetic fields from the observational as well as from a theoretical perspective. Non-radiative simulations of galaxy clusters within cosmological environment which follow the evolution of a primordial magnetic seed field have been performed using Smooth-Particle-Hydrodynamics (SPH) codes (Dolag et al. 1999, 2002, 2005) as well as Adaptive Mesh Refinement (AMR) codes (Brüggen et al. 2005; Dubois & Teyssier 2008). Although these simulations are

based on quite different numerical techniques they show good agreement in the predicted properties of the magnetic fields in galaxy clusters. When radiative cooling is included, strong amplification of the magnetic fields inside the cool-core region of clusters is found (Dubois & Teyssier 2008), in good agreement with previous work (Dolag 2000). Cosmological, magneto-hydrodynamical simulations were also performed using finite-volume and finite-difference methods. Such simulation are used to either follow a primordial magnetic field (Li et al. 2008) or the creation of magnetic field in shocks through the so-called Biermann battery effect (Kulsrud et al. 1997; Ryu et al. 1998), on which a subsequent turbulent dynamo may operate. The latter predict magnetic field strength in filaments with somewhat higher values (e.g. see Sigl et al. 2004) than predicted by simulations which follow the evolution of a primordial magnetic seed field, but in line with predictions of magnetic field values from turbulence (Ryu et al. 2008). Therefore further investigations are needed to clarify the structure, evolution and origin of magnetic fields in the largest structures of the Universe, their observational signatures as well as their interplay with other processes acting in galaxy clusters and the large scale structure.

The majority of the complexity of galaxy clusters comes from their hierarchical build up within the large-scale structure of the Universe. In order to study their formation it is necessary, to follow

* E-mail: kdolag@mpa-garching.mpg.de

a large volume of the Universe. However, one must also describe cosmic structures down to relatively small scales, thus spanning 5 to 6 orders of magnitudes in size. The complexity of the cluster atmosphere reflects the infall of thousands of smaller objects and their subsequent destruction or survival within the cluster potential. Being the source of shocks and turbulence, these processes directly act on the magnetic field causing re-distribution and amplification. Therefore realistic modelling of these processes critically depends on the ability of the simulation to resolve and follow correctly this dynamics in galaxy clusters.

Here we present the implementation of magneto hydrodynamics in the cosmological SPH code GADGET (Springel et al. 2001; Springel 2005) allowing to explore the full size and dynamical range of up-to-date cosmological simulations. GADGET also allows us to turn on the treatment of many additional physical processes which are of interest for structure formation and make interesting links with the treatment of magnetic fields for future studies. This includes thermal conduction (Jubelgas et al. 2004; Dolag et al. 2004), physical viscosity (Sijacki & Springel 2006), cooling and star-formation (Springel & Hernquist 2003), detailed modelling of the stellar population and chemical enrichment (Tornatore et al. 2004, 2007) and a self consistent treatment of cosmic rays (Enßlin et al. 2007; Pfrommer et al. 2007). The MHD implementation presented here is fully compatible with all these extensions, but here we want to focus on non-radiative simulations. This is to avoid the increased complexity and the complicated interplay of all these additional processes with structure formation and therefore its interplay with the evolution of the magnetic field.

The paper is structured as follows: In section 2 we present the details of the numerical implementation, whereas in section 3 we present various code validation tests, all performed in fully three dimensional setups. In section 4 we present the formation of a galaxy cluster as an example for a cosmological application before we present our conclusions in section 5. In addition we present a convergence test for the code in the appendix.

2 SPH-MHD IMPLEMENTATION

We have implemented the MHD equations in the cosmological SPH code GADGET (Springel et al. 2001; Springel 2005). In this section we present the relevant details of this implementation. While developing the MHD implementation made use of GADGET-1 (Springel et al. 2001) and GADGET-2 (Springel 2005), all simulations presented on this paper are based on the most recent version of the code, GADGET-3 (Springel, in prep). Note that the implementation therefore is fully parallelized and benefits from many optimizations within the general parts of the code, especially the calculation of self gravity and optimization in data structures as well as work-load balancing. Therefore, this implementation is an ideal tool to follow the evolution of magnetic fields, allowing to explore the full size and dynamical range in up-to-date cosmological simulations.

2.1 SPH implementation in GADGET

The basic idea of SPH is to discretize the fluid in mass elements (m_i), e.g. particles at positions \vec{x}_i (Lucy 1977; Gingold & Monaghan 1977). To build continuous fluid quantities, one starts with a general definition of a kernel smoothing method. The most frequently used kernel $W(|\vec{x}|, h)$ is the B_2 -Spline (Monaghan & Lattanzio 1985), which can be written as

$$W(x, h) = \frac{8}{\pi h^3} \begin{cases} 1 - 6 \left(\frac{x}{h}\right)^2 + 6 \left(\frac{x}{h}\right)^3 & 0 \leq \frac{x}{h} \leq 0.5 \\ 2 \left(1 - \frac{x}{h}\right)^3 & 0.5 \leq \frac{x}{h} \leq 1 \\ 0 & 1 \leq \frac{x}{h} \end{cases}, \quad (1)$$

It is worth stressing that, contrary to other SPH implementation, GADGET uses the notation in which the kernel $W(x, h)$ reaches zero at $x/h = 1$ and not at $x/h = 2$. The density ρ_i at each particle position \vec{x}_i can be estimated via

$$\langle \rho_i \rangle = \sum_j m_j W(\vec{x}_i - \vec{x}_j, h_i), \quad (2)$$

where the smoothing length h_i is defined by solving the equation

$$\frac{4\pi}{3} h_i^3 \rho_i = N m_i. \quad (3)$$

A typical value for N is in the range of 32-64, which correspond to the number of neighbors which are traditionally chosen in SPH implementations.

In GADGET, the equation of motion for the SPH particles are implemented based on a derivation from the fluid Lagrangian (Springel & Hernquist 2002) and take the form

$$\left(\frac{d\vec{v}_i}{dt} \right)^{(\text{hyd})} = - \sum_{j=1}^N m_j \left[f_i^{\text{co}} \frac{P_i}{\rho_i^2} \vec{\nabla}_i W_i + f_j^{\text{co}} \frac{P_j}{\rho_j^2} \vec{\nabla}_i W_j \right]. \quad (4)$$

The coefficients f_i are defined by

$$f_i^{\text{co}} = \left[1 + \frac{h_i}{3\rho_i} \frac{\partial \rho_i}{\partial h_i} \right]^{-1}, \quad (5)$$

and reflect the full, self-consistent correction terms arising from varying the particle smoothing length. The abbreviation $W_i = W(|\vec{r}_i - \vec{r}_j|, h_i)$ and $W_j = W(|\vec{r}_i - \vec{r}_j|, h_j)$ are the two kernels of the interacting particles. The pressure of each particle is given by $P_i = A_i \rho_i^\gamma$, where the entropic function A_i stays constant for each particle in the absence of shocks or other sources of heat.

To capture shocks properly, artificial viscosity is usually used. Therefore, in GADGET the viscous force is implemented as

$$\left(\frac{dv_i}{dt} \right)^{(\text{visc})} = - \sum_{j=1}^N m_j \Pi_{ij} \nabla_i \bar{W}_{ij}, \quad (6)$$

where $\Pi_{ij} \geq 0$ is non-zero only when particles approach each other in physical space. The viscosity generates entropy at a rate

$$\frac{dA_i}{dt} = \frac{1}{2} \frac{\gamma - 1}{\rho_i^{\gamma-1}} \sum_{j=1}^N m_j \Pi_{ij} \vec{v}_{ij} \cdot \nabla_i \bar{W}_{ij}, \quad (7)$$

Here, the symbol \bar{W}_{ij} denotes the arithmetic mean of the two kernels W_i and W_j .

For the parameterization of the artificial viscosity, starting with version 2 of GADGET, a formulation proposed by Monaghan (1997) based on an analogy with Riemann solutions of compressible gas dynamics, is used. In this case, the resulting viscosity term can be written as

$$\Pi_{ij} = \frac{-0.5 \alpha v_{ij}^{\text{sig}} \mu_{ij}}{\rho_{ij}} f_{ij}^{\text{shear}} \quad (8)$$

for $\vec{r}_{ij} \cdot \vec{v}_{ij} \leq 0$ and $\Pi_{ij} = 0$ otherwise, i.e. the pair-wise viscosity is only non-zero if the particles are approaching each other. Here $\mu_{ij} = \vec{v}_{ij} \cdot \vec{r}_{ij} / |\vec{r}_{ij}|$ is the relative velocity projected onto the separation vector and the signal velocity is estimated as

$$v_{ij}^{\text{sig}} = c_i + c_j - \beta \mu_{ij}, \quad (9)$$

with $c_i = \sqrt{\gamma P_i / \rho_i}$ denoting the sound velocity. In GADGET-2 the values $\alpha = 1$ and $\beta = 3$ are commonly used for the dimensionless parameters within the artificial viscosity. Here we have also included a viscosity-limiter $f_i^{\text{shear}} = (f_i^{\text{shear}} + f_j^{\text{shear}})/2$, which is often used to suppress the viscosity locally in regions of strong shear flows, as measured by

$$f_i^{\text{shear}} = \frac{|\langle \vec{\nabla} \cdot \vec{v} \rangle_i|}{|\langle \vec{\nabla} \cdot \vec{v} \rangle_i| + |\langle \vec{\nabla} \times \vec{v} \rangle_i| + \sigma_i}, \quad (10)$$

which can help to avoid spurious angular momentum and vorticity transport in gas disks (Balsara 1995; Steinmetz 1996), with the common choice $\sigma_i = 0.0001 c_i / h_i$.

This also leads naturally to a Courant-like hydrodynamical time-step

$$\Delta t_i^{(\text{hyd})} = \frac{C_{\text{courant}} h_i}{\max_j (v_{ij}^{\text{sig}})}, \quad (11)$$

where C_{courant} is a numerical constant, typically chosen to be in the range 0.15 – 0.2.

2.2 Co-moving variables and integration

The equation of motion are integrated using a leap-frog integration making use of a kick-drift-kick scheme. Within this scheme, all the pre-factors due to the cosmological background expansion are taken into account within the calculation of the kick- and drift-factors (see Springel 2005). For the integration of the entropy within a cosmological simulation, a factor $(Ha^2)^{-1} = \frac{dt}{da}$ is present in equation 7 to take into account that the internal time variable in GADGET is the expansion parameter a . All the formulation of the MHD equations within GADGET have to be adapted accordingly to this choice of variables.

2.3 Magnetic signal velocity

A natural generalization of the signal velocity v_{ij}^{sig} in the framework of MHD is to replace the sound velocity c_i by the fastest magnetic wave as suggested by Price & Monaghan (2004a). Therefore the sound velocity c_i gets replaced by

$$v_i = \frac{1}{\sqrt{2}} \left[\left(c_i^2 + \frac{B_i^2}{\mu_0 \rho_a} \right) \sqrt{\left(c_i^2 + \frac{B_i^2}{\mu_0 \rho_i} \right)^2 - 4 \frac{c_i^2 (\vec{B} \cdot \vec{r}_{ij} / |\vec{r}_{ij}|)^2}{\mu_0 \rho_i}} \right]^{0.5}. \quad (12)$$

As this new definition of the signal velocity also enters the time-step criteria (11), no extra time-step criteria due to the magnetic field has to be defined. We note that we still see improvements in the solution to the test problems, if we choose a more conservative settings within the Courant condition. Therefore we generally use $C_{\text{courant}} = 0.075$, which is halve the value usually used in pure hydrodynamical problems. Different authors also propose to use different values for α and β within the artificial viscosity definition (8). Whereas typically $\alpha = 1$ is chosen, Monaghan (1997) proposed to use $\beta = 3$. Price & Monaghan (2004a,b) propose to use $\beta = 2$ or $\beta = 1$ respectively. We find slight improvements in our test problems when using $\alpha = 2$ and $\beta = 1.5$, which we use throughout this paper. We also note, that the viscosity suppression switch f_{ij}^{shear} was introduced based on an earlier realization of the artificial viscosity and it is not clear if it is still needed. As we note

significant improvements in our test problems when neglecting this switch we do not use this switch throughout this paper. Also for the cosmological application presented in the last part of this paper, this switch was always turned off.

2.4 Induction equation

The evolution of the magnetic field is given by the induction equation,

$$\frac{d\vec{B}}{dt} = (\vec{B} \cdot \vec{\nabla})\vec{v} - \vec{B}(\vec{\nabla} \cdot \vec{v}), \quad (13)$$

if ohmic dissipation is neglected and the constraint $\vec{\nabla} \cdot \vec{B} = 0$ is used. The SPH equivalent reads

$$\frac{d\vec{B}_i}{dt} = \frac{1}{Ha^2} \frac{f_i^{\text{co}}}{\rho_i} \left[\sum_{j=1}^N m_j [\vec{B}_i(\vec{v}_{ij} \cdot \vec{\nabla}_i W_i) - \vec{v}_{ij}(\vec{B}_i \cdot \vec{\nabla}_i W_i)] - 2\vec{B}_i \right], \quad (14)$$

where $(Ha^2)^{-1} = \frac{dt}{da}$ takes into account that the internal time variable in GADGET is the expansion parameter a . Note that here, by construction, only the kernel W_i and its derivative is used. The second term $-2\vec{B}_i$ accounts for the dilution of the frozen in magnetic field due to cosmic expansion. Both these terms are only present in the cosmological simulations and absent for the code evaluation presented in section 3. In component form the induction equation reads

$$\frac{dB_i^k}{dt} = \frac{1}{Ha^2} \frac{f_i^{\text{co}}}{\rho_i} \left[\sum_{j=1}^N m_j (v_{ij}^k B_i^l - B_i^k v_{ij}^l) \frac{\partial W_i}{\partial u} \frac{\vec{r}_{ij}^l}{|\vec{r}_{ij}|} \right] - 2\vec{B}_i^k. \quad (15)$$

Note that, as also suggested by Price & Monaghan (2004b), we wrote down the equations including the correction factor f_i^{co} which reflects the correction terms $(\frac{dW}{dh})$ arising from the variable particle smoothing length. Unfortunately it is not possible to directly infer the exact form the correction factors from first principles for the induction equation. However, Price & Monaghan (2004b) showed that, if not chosen in the same way as for the Lorenz force, inconsistency between the induction equation and magnetic force arrives. The effect of these factors in the induction equation is quite small, but nevertheless one notices tiny improvements in test problems when they are included. Therefore, we included them for all our applications presented in this paper.

2.5 Magnetic force

The magnetic field acts on the gas via the Lorenz force, which can be written in a symmetric, conservative form involving the magnetic stress tensor (Phillips & Monaghan 1985)

$$M_i^{kl} = \left(\vec{B}_i^k \vec{B}_i^l - \frac{1}{2} |\vec{B}_i|^2 \delta^{kl} \right). \quad (16)$$

The magnetic contribution to the acceleration of the i -th particle can therefore be written as

$$\left(\frac{d\vec{v}_i}{dt} \right)^{(\text{mag})} = \frac{a^{3\gamma}}{\mu_0} \sum_{j=1}^N m_j \left[f_i^{\text{co}} \frac{M_i}{\rho_i^2} \cdot \vec{\nabla}_i W_i \right]$$

$$+ f_j^{\text{co}} \frac{M_j}{\rho_j^2} \cdot \vec{\nabla}_j W_j \Big]. \quad (17)$$

Here $a^{3\gamma} = \frac{dt}{d\eta}$ is needed to transform the equations to the internal variables for cosmological simulations and is set to one in all other cases. Also μ_0 has to be chosen properly (see section 2.9). The factors f_i^{co} reflect the correction terms ($\frac{dW}{dh}$) arising from the variable particle smoothing length as introduced already (see also Price & Monaghan 2004b). In component form the equation reads

$$\left(\frac{d\vec{v}_i^k}{dt} \right)^{(\text{visc})} = \frac{a^{3\gamma}}{\mu_0} \sum_{j=1}^N m_j \left[f_i^{\text{co}} \frac{M_i^{kl}}{\rho_i^2} \frac{\partial W_i}{\partial u} \frac{\vec{r}_{ij}^k}{|\vec{r}_{ij}|} + f_j^{\text{co}} \frac{M_j^{kl}}{\rho_j^2} \frac{\partial W_j}{\partial u} \frac{\vec{r}_{ij}^k}{|\vec{r}_{ij}|} \right]. \quad (18)$$

It is well known that this formulation becomes unstable for situations, in which the magnetic forces are dominating (Phillips & Monaghan 1985). The reason for this is that the magnetic stress can become negative, leading to the clumping of particles. Therefore, some additional measures have to be taken to suppress the onset of this instability.

2.6 Instability corrections

There are several methods proposed in the literature to suppress the onset of the clumping instability which is caused by the implementation of the magnetic force. However their ability was found to depend on the details of the simulation setup. In the next sections we will briefly discuss the different possibilities in the context of building up a implementation for cosmological simulations.

2.6.1 Adding a constant value

One method to remove the instability was pointed out by Phillips & Monaghan (1985), who suggested to calculate the maximum of the magnetic stress tensor and to subtract it globally from all particles. Or similar, as suggested in Price & Monaghan (2005), to subtract the contribution of a constant magnetic field. This is simple and straight forward if there is a strong, external magnetic field contribution from the initial setup, which can be associated with the term one subtracts. However, with cosmological simulations in mind, this approach is not very viable and therefore we did not use this approach.

2.6.2 Anti clumping term

Monaghan (2000) suggested the introduction of an additional term in the momentum equation which prevents particles from clumping in the presence of strong magnetic stress. Including this term, equation (16) reads

$$M_i^{kl} = \left(\vec{B}_i^k \vec{B}_i^l - \frac{1}{2} |\vec{B}_i|^2 \delta^{kl} - R_i \vec{B}_i^k \vec{B}_i^l \right), \quad (19)$$

where R_i is a steepened kernel which can be defined as

$$R_i = \frac{\epsilon}{2} \left(\frac{W_i}{W_1} \right)^n. \quad (20)$$

The modification of the kernel is made so that contributions are significant only at distances below the average particle spacing u_1 , so W_1 is defined as $W_1 = W(u_1)$. Typical values for the remaining parameters are $\epsilon = 0.8$ and $n = 5$. This method was also used in Price & Monaghan (2004a,b) whereas they found $u_1 = 1.5h$ to

be a good choice for 1D simulations and switched to $u_1 = 1.1h$ for 2D simulations. In agreement with Price & Monaghan (2005) we find that in 3D and allowing the smoothing length to vary, this approach does not help to suppress the instabilities very efficiently. We therefor did not use this approach within this work.

2.6.3 $\text{div}(\vec{B})$ force subtraction

Børve et al. (2001) suggested explicitly subtracting the effect of any numerically non-vanishing divergence of \vec{B} . Therefore, one can explicitly subtract the term

$$\left(\frac{d\vec{v}_i^k}{dt} \right)^{(\text{corr})} = -a^{3\gamma} \frac{1}{\mu_0} \hat{\beta} \vec{B}_i^k \sum_{j=1}^N m_j \left[f_i^{\text{co}} \frac{\vec{B}_i^l}{\rho_i^2} \cdot \vec{\nabla}_i W_i + f_j^{\text{co}} \frac{\vec{B}_j^l}{\rho_j^2} \cdot \vec{\nabla}_j W_j \right] \quad (21)$$

from the momentum equation. Here again, $a^{3\gamma} = \frac{dt}{d\eta}$ and μ_0 are introduced to transform the equation to the internal units used. To be consistent with the other formulations, we included f_i^{co} , which are the $\frac{dW}{dh}$ terms. In the original work (Børve et al. 2001), $\hat{\beta} = 1$ was chosen. In component form this equation reads

$$\left(\frac{d\vec{v}_i^k}{dt} \right)^{(\text{corr})} = -a^{3\gamma} \frac{1}{\mu_0} \hat{\beta} \vec{B}_i^k \sum_{j=1}^N m_j \left[f_i^{\text{co}} \frac{\vec{B}_i^l}{\rho_i^2} \frac{\partial W_i}{\partial u} \frac{\vec{r}_{ij}^k}{|\vec{r}_{ij}|} + f_j^{\text{co}} \frac{\vec{B}_j^l}{\rho_j^2} \frac{\partial W_j}{\partial u} \frac{\vec{r}_{ij}^k}{|\vec{r}_{ij}|} \right]. \quad (22)$$

In principle, this term breaks the momentum conservation form of the MHD formulation. However, in practice, this seems to be a minor effect. Børve et al. (2004) argued that stability for linear waves in 2D can be safely reached even when not subtracting the full term but choosing $\hat{\beta} < 1$; e.g. they suggested $\hat{\beta} = 0.5$ to further minimizing the non-conservative contribution. However, it is not clear if this stays true for 3D setups and in the non-linear regime. Additionally, Børve et al. (2004) used a higher order kernel and therefore it is also not clear if that is still true in our case. As the results in our test problems seem unharmed by the possible violation of momentum conservation due to the formulation of the correction factor in the Lorenz force, we keep it in the form suggested in earlier work (e.g. Børve et al. 2001).

In Børve et al. (2006) a more general formalism to obtain $\hat{\beta}$ for each particle was introduced with the aim to further minimize the violation of momentum conservation in the formulation of the correction terms in the Lorenz force. Unfortunately, in the light of cosmological simulation, this seems not to be very practical as it contains a scan for a maximum value over all particles, which in a cosmological context makes no sense as there is not a specific single object to which such characteristics can be tuned to.

In general we find that this correction term significantly improves all results in our test simulations and effectively suppresses the onset of the clumping instability. It was also already successfully used in previous, cosmological applications (e.g. Dolag et al. 2004; Rordorf et al. 2004; Dolag et al. 2005).

2.7 Regularization schemes

Beside instabilities, noise (e.g. fluctuations of the magnetic field imprinted by numerical effects when integrating the induction equation) is a source of errors in SPH-MHD implementations.

Here, the entropy conserving formalism of the underlying SPH implementation contributes to a significant improvement of the MHD formalism compared to previous MHD implementations in SPH by generally improving the density estimate and the calculation of derivatives. It has to be noted, that this is not only due to the $\frac{dW}{dh}$ terms, but in large part also from the new formalism for calculating of the smoothing length. As described before, the smoothing length h_i for each particle is no longer calculated by counting neighbors within the sphere, but by solving equation (3) and therefore, for a formal number of neighbors N , there exist only one unambiguous value of h_i . Note that, as this equation is solved iteratively, it is usual to give some allowed range of N , however in our case we can choose the range smaller than 1 and typically we use $N = 64 \pm 0.1$. Regularization schemes therefore are either based on improving the calculation of the interactions to reduce the creation of small irregularities arising from numerical effects or on removing small irregularities.

2.7.1 Particle splitting

Børve et al. (2001) developed a scheme to regularize the interaction of particles in SPH based on a discretization of the smoothing length h_i by factors of 2. In such cases, interactions between two particles with different smoothing length can be realized by splitting the one with the larger smoothing length into 2^n (where n is the dimensionality) particles, placed on a 2^n sub-grid. Such split particles then have the same smoothing length as the particles with which they interact. Originally this scheme was invented to avoid the problems induced by a variable smoothing length (before the correction terms were properly introduced in SPH) and gave good results in 1D and 2D (see Børve et al. 2001, 2004, 2006). However, in 3D the step in neighbors is quite large when quantizing the smoothing length by factors of 2 and therefore the additional sampling noise by particles, especially those with small numbers of neighbors which not yet reached the point at which the smoothing length can be increased, is quite large. In fact, unfortunately, this effect is much larger than the gain in accuracy by the regularization, at least when based on standard SPH formalism, (see Del Pra 2003). Also, as the $\frac{dW}{dh}$ terms formally take care of all correction terms induced in the formalism when allowing a variable smoothing length, this splitting – and specifically the quantization of the smoothing length – is no longer needed. This might be different when further improving the SPH (and specially the MHD) method. For example when re-mapping techniques based on Voronoi tessellation are used (e.g. Børve et al. 2006), or special coordinates like spherical or cylindrical are used (e.g. Omang et al. 2006).

2.7.2 Smoothing the magnetic field

Another method to remove small scale fluctuations and to regularize (e.g. to obtain a magnetic field which does not show strong fluctuations below the smoothing length) the magnetic field is to smooth the magnetic field periodically. As suggested by Børve et al. (2001), one can calculate a smoothed magnetic field $\langle \vec{B}_i \rangle$ for each particle,

$$\langle \vec{B}_i \rangle = \frac{\sum_j \frac{m_j}{\rho_j} \vec{B}_j W_i}{\sum_j \frac{m_j}{\rho_j} W_i}. \quad (23)$$

Then, in periodic intervals, one can calculate a new, regularized magnetic field by

$$\vec{B}_i^{\text{new}} = q \langle \vec{B}_i \rangle + (1 - q) \vec{B}_i. \quad (24)$$

Note that this, in principal, acts similar to the mixing process on resolution scale present in Eulerian schemes. However, introduced in this way, the amount of mixing (e.g. dissipation) of magnetic field depends on the frequency with which this procedure is applied and the value of q chosen. Typically, we set q to one and perform the smoothing at ever 15^{th} - 20^{th} main time-step. It is worth to mention that implemented in this form, total energy is not conserved (as magnetic field fluctuations on scales smaller than the smoothing length are just removed) and, as the time-steps depend on the chosen resolution, this method is even resolution dependent. Never-the-less it leads to improvements in the results of our test problems, without strongly smoothing sharp features. It also works without problem in 3D and has already been used in cosmological simulations (Dolag et al. 2004, 2005).

2.7.3 Artificial magnetic dissipation

Another possibility to regularize the magnetic field was presented by Price & Monaghan (2004a), who suggested including an artificial dissipation for the magnetic field, analogous to the artificial viscosity used in SPH. In Price & Monaghan (2004a) it was suggested that the dissipation terms be constructed based on the magnetic field component perpendicular to the line joining the interacting particles. However, to better suppress the small scale fluctuations within the magnetic field which appear due to numerical effects especially in multi-dimensional tests, Price & Monaghan (2004b) suggested basing the artificial dissipation on the change of the total magnetic field rather than on the perpendicular field components only. We also found this to work significantly better in our test cases and therefore only use the later implementation throughout this paper. Such an artificial dissipation term can be included in the induction equation as

$$\left(\frac{d\vec{B}_i}{dt} \right)^{(\text{diss})} = \frac{1}{Ha^2} \frac{\rho_i \alpha_B}{2} \sum_{j=1}^N \frac{m_j v_{ij}^{\text{sig}}}{\hat{\rho}_{ij}^2} (\vec{B}_i - \vec{B}_j) \frac{\vec{r}_{ij}}{|\vec{r}_{ij}|} \cdot \vec{\nabla}_i W_i. \quad (25)$$

As in the induction equation before, $(Ha^2)^{-1} = \frac{dt}{da}$ takes into account that the internal time variable for cosmological simulations and is set to one in all other cases. The parameter α_B is used to control the strength of the effect, typical values are suggested to be around $\alpha_B \sim 0.5$. Similar to the artificial viscosity, this will create entropy at the rate

$$\left(\frac{dA_i}{dt} \right)^{(\text{diss})} = - \frac{\gamma - 1}{\rho_i^{\gamma-1}} \frac{\alpha_B}{4\mu_0} \sum_{j=1}^N \frac{m_j v_{ij}^{\text{sig}}}{\hat{\rho}_{ij}^2} (\vec{B}_i - \vec{B}_j)^2 \frac{\vec{r}_{ij}}{|\vec{r}_{ij}|} \cdot \vec{\nabla}_i W_{ij}. \quad (26)$$

The pre-factor $(\gamma - 1)/(\rho_i^{\gamma-1})$ properly converts the dissipation term to a change in entropy.

This method reduces noise significantly. However, depending on the choice of α_B , it can also lead to smearing of sharp features. To avoid this outside of strong shocks (e.g. where this is needed), Price & Monaghan (2005) proposed evolving α_B for each particle, similar to the handling of the time dependent viscosity as suggested by Morris & Monaghan (1997). Such, evolution of α_B for each particle will be followed by integrating

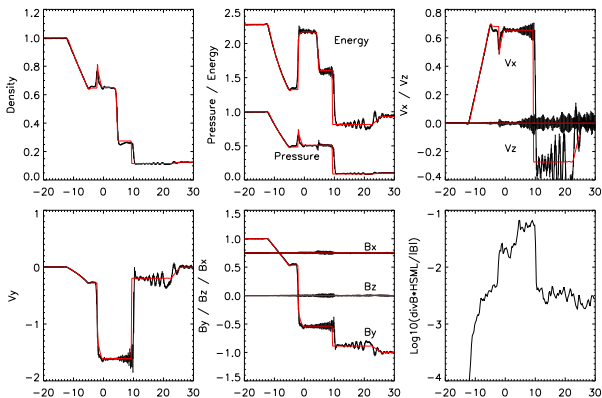


Figure 1. Test 5A at time $t = 7$ with the MHD implementation similar to that used in Dolag et al. (1999, 2002), but already including the instability correction due to subtraction of the $\text{div}(\vec{B})$ term in the force equation and in a fully three-dimensional setup. Shown in the first row are the density (left panel), total energy and pressure (middle panel) and the x, z component of the velocity field (right panel). The second row shows the y -component in the velocity field (left panel), the three components of the magnetic field (middle panel) and the measure of the $\text{div}(\vec{B})$ error, see equation (33), in the right panel. The black lines with error bars show the SPH results, the red lines are the reference results obtained with Athena in a 1D setup.

$$\frac{d\alpha_B}{dt} = -\frac{(\alpha_B - \alpha_B^{\min})}{\tau} + S, \quad (27)$$

where the source term S can be chosen as

$$S = S_0 \max\left(\frac{|\vec{\nabla} \times \vec{B}|}{\sqrt{\mu_0 \rho}}, \frac{|\vec{\nabla} \cdot \vec{B}|}{\sqrt{\mu_0 \rho}}\right) \quad (28)$$

(see Price & Monaghan 2005). The time-scale τ defines how fast the dissipation constant decays. Taking the signal velocity, one can translate this directly into a distance to the shock over which the dissipation constant decays. A useful choice of τ can be written as

$$\tau = \frac{h_i}{C v_{\text{sig}}}, \quad (29)$$

where the constant C typically is chosen to be around 0.2, allowing the dissipation constant to decay within a time that corresponds to the shock travelling 5 kernel lengths (see Price & Monaghan 2004a),

2.8 Euler potential

A very elegant way to implement the MHD equations in Lagrangian codes is the usage of so called *Euler potentials* (see Rosswog & Price 2007, and references therein). They are build as two independent variables α and β and correspond to an implicit choice of a gauge for the vector potential. They can be thought of as labels of magnetic field lines and will be advected with the flow. In this formulation, the magnetic field at any time can be represented as

$$\vec{B} = \vec{\nabla}\alpha \times \vec{\nabla}\beta. \quad (30)$$

In principle, having obtained the magnetic field, one could use this magnetic field also in the equation of motion as before. However, here we only use this simple description as a reference to check the effect of numerically non-zero divergence in the standard implementation. The evolution of the magnetic field using Euler potentials can be seen as an upper bound on amplification processes (as

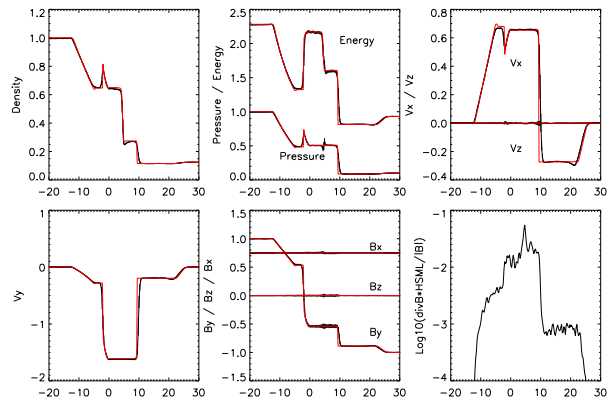


Figure 2. As figure (1), but including the magnetic waves in the signal velocity and turning of the shear viscosity suppression as explained in the code description. The main advantage are a significant reduction in the noise, specifically in the velocity, but also in the magnetic field. Also the $\text{div}(\vec{B})$ errors are reduced by a factor of ≈ 2 .

back reaction is neglected and no instabilities should be present). Therefore one can easily check the amount of artificial amplification of magnetic field within cosmological simulations.

2.9 Units and co-moving variables

In GADGET-2 the unit system is defined by setting LENGTH, MASS and VELOCITY factors with respect to the CGS system. Thereby the internal units of ENERGY and TIME are defined. The magnetic field units are defined as GAUSS. Therefore μ_0 within the MHD equations becomes to

$$\mu_0 = \frac{[\text{TIME}]^2 [\text{LENGTH}]}{4\pi [\text{MASS}]}. \quad (31)$$

Note that, for cosmological simulations, the parameterization of the units for LENGTH, MASS and TIME contain the Hubble constant h and therefore μ_0 has to be modified to be

$$\mu_0 = \frac{[\text{TIME}]^2 [\text{LENGTH}]}{4\pi [\text{MASS}] h^2}. \quad (32)$$

3 TEST PROBLEMS

To test performance of the code and to infer the optimal numerical settings for the regularization schemes, we performed the series of shock-tube problems as presented by Ryu & Jones (1995). Specially the test 5A, which is also used in Brio & Wu (1988) was used to show the effects of different numerical treatments. Additionally we performed several 2D test cases including the *Fast Rotor* test (Tóth 2000; Londrillo & Del Zanna 2000; Balsara & Spicer 1999), a *Strong Blast* (Londrillo & Del Zanna 2000; Balsara & Spicer 1999) and the *Orzang-Tang Vortex* (Orzang & Tang 1979; Dai & Woodward 1994; Picone & Dahlburg 1991; Londrillo & Del Zanna 2000). To obtain results under realistic circumstances, we performed all the tests by setting up a fully three-dimensional particle distribution. We also avoid starting from regular grids but used glass-like (White 1996) initial particle distributions instead, to get a more realistic setup. For all tests we used the same particle masses, independent of the initial density. Therefore, typical initial particle distributions for the shock-tube

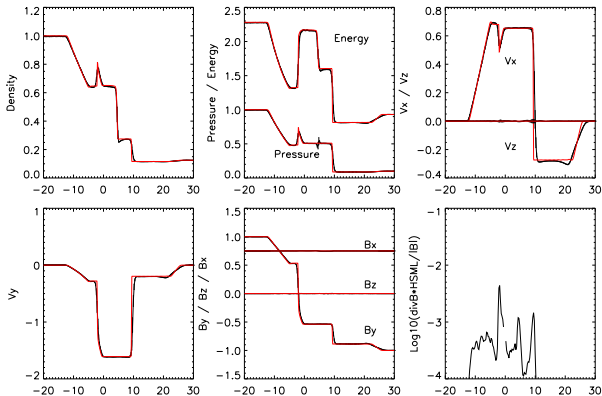


Figure 3. As figure (2), but including the regular smoothing of the magnetic field as a regularization scheme. This MHD-SPH implementation basically reflects the one used in Dolag et al. (2004, 2005). The main advantages are a further, significant reduction in the noise as well as a strong reduction of the $\text{div}(\vec{B})$ errors by a factor of ≈ 10 .

tests were based on 5^3 particles in low density and 10^3 particles in high density regions within unit volume. Usually, these unit volumes are then replicated 35 times along the x direction each. For some test cases with strong (and therefore fast) shocks, we evolved the simulations longer. In such cases we doubled the simulation setup size in the x -direction.

We assume ideal gas (e.g. $\gamma = 5/3$) and, as described before, use an equivalent of 64 neighbors for calculating the SPH smoothing length. This ensures that, in the low density regions, the SPH particles get smoothed over a region corresponding to a unit length. The number of resolution elements corresponding to a unit length therefore ranges from 1 to 4, depending whether one associates the smoothed region or the mean inter-particle distance with the effective resolution in SPH. In general, SPH converges somewhat slower compared to grid codes when comparing simulations with the same number of grid cells as SPH particles (see Appendix A for an example).

For the SPH results we usually plot the mean within a 3D slab corresponding to the smoothing length and (as error bars) the RMS over the individual particles within this volume. The reference solution was obtained using Athena (Stone et al. 2008) with typically 10-20 resolution elements per unit length, depending on the individual test. As one criteria of the goodness of the SPH simulation result we use the usual measure for the non-vanishing divergence of the magnetic field,

$$E_{\nabla\vec{B}} = \text{div}(\vec{B}) \frac{h}{|\vec{B}|}. \quad (33)$$

3.1 Shock tube 5A

The most commonly used MHD shock-tube test is the one used by Brio & Wu (1988), e.g. test 5A in Ryu & Jones (1995). The reason for this is that it involves a shock and a rarefaction of the same family moving together. Therefore it allows simultaneous testing of the code in different regimes.

Figure (1) shows the result for a code implementation similar to the first implementation used to study galaxy clusters (e.g. see Dolag et al. 1999, 2002). In addition, the instability correction due to subtraction of the $\text{div}(\vec{B})$ term was used in the force equation. Various hydro-dynamical variables at the final time (e.g. $t = 7$

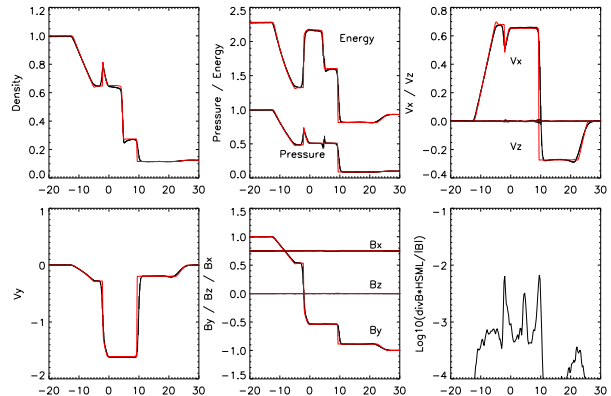


Figure 4. As figure (2), but including artificial magnetic dissipation as a regularization scheme. Similar to the smoothing of the magnetic field, significant reduction in the noise as well as a strong reduction of the $\text{div}(\vec{B})$ errors by a factor of ≈ 10 is obtained compared to the *standard* implementation.

in this case) are shown. The black lines with error bars show the MHD-SPH result, the red lines are the reference result obtained with Athena in a 1D setup. Shown are (from upper left to the bottom right panel) the density, total energy and pressure, the x - and z -component of the velocity field, the y -component in the velocity field, the three components of the magnetic field and the measure of the $\text{div}(\vec{B})$ error, obtained from equation (33). Here we also switched back to the old formulation of the artificial viscosity. Although the MHD-SPH results in general follow the solution obtained with Athena, there is a large scatter in the individual particle values within the 3D volume elements, as well as some instability, especially in the low-density part. But note that although the mean values for the internal energy, as well as the velocity or magnetic field, can locally show some systematic deviations from the ideal solution, the total energy shows much better nearly unbiased, behaviour. This demonstrates the highly conservative nature of the symmetric formulations in SPH-MHD.

Noticeable reduction of noise is obtained when using the signal-velocity based artificial viscosity and including the magnetic waves in the calculation of the signal velocity. Therefore, the magnetic waves are directly captured for the time step calculation and in the artificial viscosity, needed to capture shocks. Also switching off the shear viscosity suppression again leads to significant reduction in scatter. This can be seen in figure (2), where the noise in the velocity as well as in the magnetic field components is significantly reduced. Values of $\text{div}(\vec{B})$ are also reduced (by a factor of ≈ 2) compared to before. In general, the MHD-SPH implementation gains from the new, entropy conservation formulation of SPH, including the $\frac{dW}{dh}$ terms and the new way to determine the SPH smoothing length, both contributing to a reduction of noise (and $\text{div}(\vec{B})$) in the general treatment of hydro-dynamics by the SPH formalism. We will refer to this implementation of MHD-SPH as *standard* further on in this paper.

3.2 The effect of regularization

As described in section (2.7), there are several suggestions for regularization to the magnetic field. Here we will show results obtained by two regularization methods, namely smoothing the magnetic field in regular intervals and including an artificial dissipation.

For the first method, the magnetic field is smoothed using

TEST Nr.	Left			Right				
	ρ	V	B	P	ρ	V	B	P
— 1A —	1.00	[10.0, 0.0, 0.0]	[5.0, 5.0, 0.0]/(4 π) ²	20.0	1.000	[-10.0, 0.0, 0.0]	[5.0, 5.0, 0.0]/(4 π) ²	1.00
— 1B —	1.00	[0.0, 0.0, 0.0]	[3.0, 5.0, 0.0]/(4 π) ²	1.0	0.100	[0.0, 0.0, 0.0]	[3.0, 2.0, 0.0]/(4 π) ²	10.0
— 2A —	1.08	[1.2, 0.01, 0.5]	[2.0, 3.6, 2.0]/(4 π) ²	0.95	1.000	[0.0, 0.0, 0.0]	[2.0, 4.0, 2.0]/(4 π) ²	1.00
— 2B —	1.00	[0.0, 0.0, 0.0]	[3.0, 6.0, 0.0]/(4 π) ²	1.0	0.100	[0.0, 2.0, 1.0]	[3.0, 1.0, 0.0]/(4 π) ²	10.0
— 3A —	1.00	[50.0, 0.0, 0.0]	-[0.0, 1.0, 2.0]/(4 π) ²	0.4	0.100	[0.0, 0.0, 0.0]	[0.0, 1.0, 2.0]/(4 π) ²	0.20
— 3B —	0.10	[-1.0, 0.0, 0.0]	[0.0, 1.0, 0.0]	1.0	1.000	[1.0, 0.0, 0.0]	[0.0, 1.0, 0.0]	1.00
— 4A —	1.00	[0.00, 0.0, 0.0]	[1.0, 1.0, 0.0]	1.0	0.200	[0.0, 0.0, 0.0]	[1.0, 0.0, 0.0]	0.10
— 4B —	0.40	[-0.669, 0.986, 0.0]	[1.3, 0.0025293, 0.0]	0.5247	1.000	[0.0, 0.0, 0.0]	[1.3, 1.0, 0.0]	1.00
— 4C —	0.65	[0.667, -0.257, 0.0]	[0.75, 0.55, 0.0]	0.50	1.000	[0.4, -0.94, 0.0]	[0.75, 0.00001, 0.0]	0.75
— 4D —	1.00	[0.0, 0.0, 0.0]	[7.0, 0.001, 0.0]	1.0	0.300	[0.0, 0.0, 0.0]	[7.0, 1.0, 0.0]	0.20
— Brio Wu —	1.00	[0.0, 0.0, 0.0]	[0.75, 1.0, 0.0]	1.0	0.125	[0.0, 0.0, 0.0]	[0.75, -1.0, 0.0]	0.10

Table 1. Summary table with the initial conditions of the left and right side of the shock tubes.

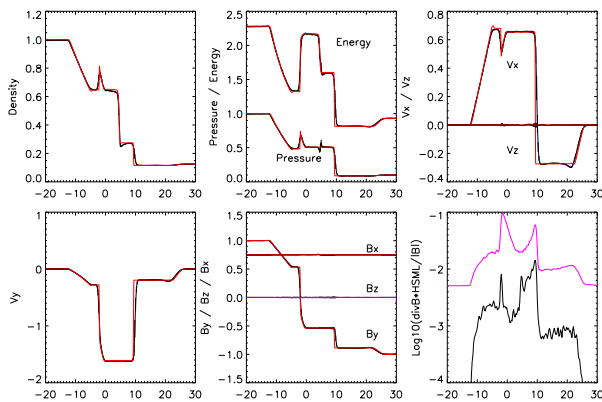


Figure 5. As figure (2), but including time dependent artificial magnetic dissipation as a regularization scheme. No significance improvement is obtained. Note that here in the lower right panel the artificial dissipation constant (α_B) is shown. The effect of suppressing the dissipation is clearly visible, and the maximum value is only reached in peaks associated with the region of strong shocks. However the improvement in the smearing of sharp features is not very significant.

the same kernel as used for the normal SPH calculations. In this case, there are two numerical parameter one can choose. One is q in equation (24), which quantifies the weight with which the smoothed component enters into the updated magnetic field. We always use $q = 1$ here, which means that we completely replace the magnetic field by the smoothed value. The second is T_{BS} , which is the time interval at which the smoothing is done. Here we use a value corresponding to a smoothing every 30th global time step. This correspond to the SPH-MHD implementation used to study the magnetic field in clusters and large scale structure within the local universe, see Dolag et al. (2004, 2005). Figure (3) shows the result for the same shock-tube test as before. Clearly, the noise in the individual quantities is strongly reduced. Also the error in $\text{div}(\vec{B})$ is reduced by more than one order of magnitude. Note that the error bars for the MHD-SPH implementation are of the size of the line width or smaller in most of the cases and therefore no longer clearly visible. However, one can notice some small effect of smearing sharp features. Additionally, some states – like the region with the negativ x -component of the velocity behind the the fast rarefaction wave propagating to the right – converge to values which have small but systematic deviations from the exact solution.

In the second method, the magnetic field can be dissipated in the same way as artificial dissipation works in the hydrodynamics. Here the numerical parameter one has to chose is the strength of this artificial, magnetic dissipation α_B in equation (25) and (26). Figure (4) shows the result for the same shock-tube test as before using $\alpha_B = 0.1$. Similar to the first method presented, the noise in the individual quantities is strongly reduced and also the error in $\text{div}(\vec{B})$ is reduced by one order of magnitude. Again, the error bars are smaller than the line width nearly everywhere. Also, some small effects of smearing sharp features are visible as well as some small but systematic deviations from the exact solution. In general, this method works slightly better than the smoothing of the magnetic field, but the differences are generally small.

One idea to reduce the unwanted side effects of such regularization schemes was presented in Price & Monaghan (2005) and is based on a modification of the artificial, magnetic dissipation constant α_B . Thereby, every particle evolves its own numerical constant, so that this value can decay outside the regions needed and therefore the effects of the artificial dissipation are suppressed outside the regions where it is needed. Figure 5 shows the same test as before, but this time where α_B evolves for each particle, as shown in the lower right panel. Clearly, the values are strongly reduced outside the regions associated with sharp features (e.g. shocks), but the effect of smearing sharp features and the small offset of some states are not significantly reduced. This is because in the region in which these side effects originate, the dissipation is still working with its maximum numerical value.

3.3 Shock tube problems

As can be seen in figures (3) and (4), the side effects of smoothing features by the different regularization methods depend on the details of the underlying structure of the shock-tube test. Even more interesting, the states where one can see small deviations from the ideal solution are different for the two different regularization methods. Therefore we performed the full set of different shock-tube tests as presented in Ryu & Jones (1995) to test the overall performance as well as the different implementations under different circumstances. The four test families deal with different complexities of velocity and magnetic field structures, leading to different kind of waves propagating. A summary of the results of these tests can be found in figure (6). Plotted are the total energy (left panels), the velocity along the x -direction (middle panels) and the magnetic field along the y -direction (right panels). The red lines re-

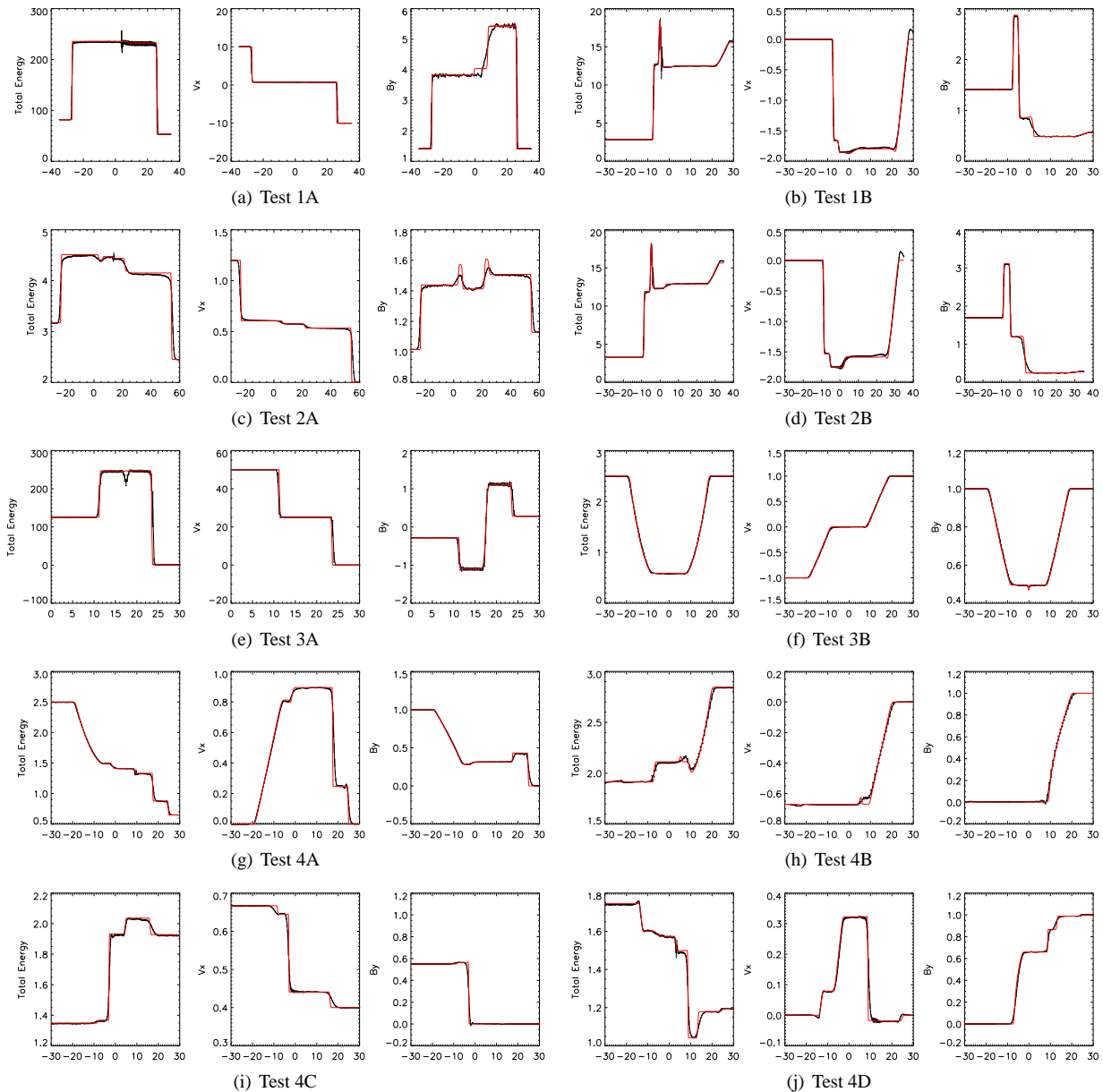


Figure 6. Representative plots of the additional 10 shock-tube tests from Ryu & Jones (1995). Shown for each test are the total energy (left panels), the velocity along the x -direction (middle panels) and the magnetic field along the y -direction (right panels).

flects the ideal solution obtained with Athena, the black lines with error bars mark the results from the SPH-MHD implementation using the magnetic field smoothing every 30th main time step. Note that the error bars in most cases are smaller than the line width. The initial setups for the shock-tube tests can be found in table 1, which lists the state vector of the left and right states for the different shock tube tests.

The first family of tests ($1A/1B$) has no structure in the tangential direction of the propagating shocks in magnetic field and velocity, e.g. $B_z = v_z = 0$. As we expect, in the $1A$ test, the strong shock (large jump in v_x) leads to some visible noise in the magnetic field component B_y , also translating into significant noise in the total energy. The regularization method here suppresses the formation of the intermediate state in B_y in the SPH-MHD implementation, as can be seen in figure 6(a). The second case, the $1B$ test, the weak

shock is captured well. Again in some regions some smearing of sharp features due to the regularization method is clearly visible.

The second class of shocks ($2A/2B$) involve three dimensional velocity structures, where the plane of the magnetic field rotates. All features (e.g. fast/slow shocks, rotational discontinuity and fast/slow rarefaction wave, for details see Ryu & Jones (1995)), are well captured, see figure 6(c) and 6(d). Some of the features are clearly smoothed by the regularization method.

The third class of tests ($3A/3B$) shows handling of magnetosonic structures. The first has a pair of magnetosonic shocks with zero parallel field and the second are magnetosonic rarefactions. Although there is slightly more noise present, all states are captured extremely well, except the numerical feature left at the position dividing the two states initially, see figure 6(e) and 6(f).

The fourth test family ($4A/4B/4C/4D$) deals with the so-called

switch-on and switch-off structures. The tangential magnetic field turns on in the region behind switch-on fast shocks and switch-on slow rarefactions. Conversely, in the switch-off slow shocks and switch-off fast rarefactions the tangential magnetic field turns off. Again, all structures are captured well with the exception of one feature in figure 6(h), where clearly the regularization leads to wash-out's one state. Otherwise the regularization leads to smoothing of some structures similar to the tests presented before.

In general, figure 6 demonstrates that all these different situations have to be included when trying to measure the performance and quality of different implementations of regularization methods.

3.4 Finding optimal numerical parameters

To optimize, we performed all these 11 shock-tube tests with various different settings for the parameters in the regularization methods and evaluated the quality of the result obtained with the MHD-SPH implementation. To measure this, we used two estimators. First, we have chosen the mean of all $\text{div}(\vec{B})$ errors within the simulation region shown in the plots, as defined by

$$\Delta_{\text{div}(\vec{B})} = \left\langle \text{div}(\vec{B}) \frac{h}{|\vec{B}|} \right\rangle_x. \quad (34)$$

Second, we measured the discrepancy of the MHD-SPH result for the magnetic field relative to the results obtained by Athena. Therefore we calculate first

$$\delta_{B^i}(x) = \frac{(\vec{B}_{\text{SPH}}^i(x) - \vec{B}_{\text{Athena}}^i(x))^2}{\text{RMS}_{B^i}^2(x)} \quad (35)$$

for each component i of the magnetic field \vec{B} within each 3D slab corresponding to the smoothing length. The RMS of B^i reflects the noise of B_i within the chosen slab. We then calculate

$$\hat{\Delta}_{B^i} = \left(\sum_x \delta_{B^i}(x) \right) \left(\sum_x \text{RMS}_{B^i}^2(x) \right), \quad (36)$$

for each component of the magnetic field. This includes both contributions, the deviation of the MHD-SPH from the ideal solution as well as the noise within each 3D slab of the MHD-SPH implementation. To judge the improvement of the regularization methods we sum up all three components and further relate this measurement to the value obtained with the *standard* implementation, e.g.

$$\Delta_B = \frac{\sum_i \hat{\Delta}_{B^i}}{\sum_i \hat{\Delta}_{B^i}^{\text{std}}} - 1. \quad (37)$$

We will use these two error estimators, $\Delta_{\text{div}(\vec{B})}$ and Δ_B , to measure the quality of the individual MHD-SPH implementations.

3.4.1 Regularization by smoothing the magnetic field

Choosing the time interval between smoothing the magnetic field is a compromise between reducing the noise in the magnetic field components (as well as reducing $\text{div}(\vec{B})$) by smoothing more often and preventing sharp features from smearing out by more rarely smoothing. Figure 7 shows a summary of the results of the individual shock-tube test computed with different smoothing intervals. As expected, when using shorter smoothing intervals the error in $\text{div}(\vec{B})$ reduces. For the quality measure of the SPH-MHD implementation the situation changes. Short smoothing intervals generally increase the discrepancy, many of them even to larger values

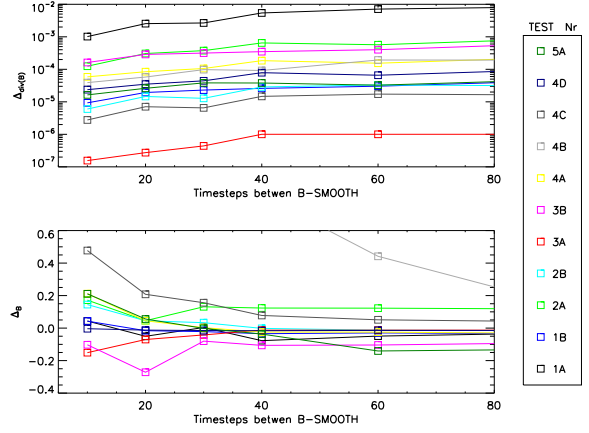


Figure 7. Shown are the mean error in divergence (upper panel) and the measure of the quality (lower panel) as defined in equation (37) obtained by the MHD-SPH implementation for different values of the smoothing interval. The different lines are for the 11 different shock-tube tests as indicated by the labels.

than the *standard* run. Specifically *4B* and *4C* show strong deviations due to smearing of sharp features. Note that the non-monotonic behavior shown in some tests usually relates to some residual resonances between the magnetic waves and the smoothing intervals in the noise. Some tests show a minima in the differences at smoothing intervals around 20. The test *3A* seems to prefer even shorter smoothing intervals. In general, values around 20-30 seem to be a good choice.

3.4.2 Artificial dissipation

As before, choosing the value for the artificial magnetic dissipation constant α_B is a compromise between reducing the noise in the magnetic field components (as well as reducing $\text{div}(\vec{B})$) and preventing sharp features from smearing out due to the effect of the dissipation. Figure 8 shows a summary of the results of the individual shock-tube tests computed with different values for the artificial magnetic dissipation. As expected, using larger values reduces the error in $\text{div}(\vec{B})$ significantly. Similar to before, using larger values also generally results in an increase of the discrepancy between the SPH MHD implementation and the true solution, again usually to even larger values than in the *standard* run. As before, especially the shock-tube test *4B* and *4C* show strong deviations due to smearing of sharp features. Note that here less non-monotonic behavior is visible (except for test *4B*). The main reason is that dissipation is a continuous process, so resonances between dissipation and the magnetic waves cannot be very pronounced. Taking all tests into account, a good choice for α_B seems to be around 0.1.

3.4.3 Time dependent artificial dissipation

One idea to reduce the effect of the artificial dissipation is to make the artificial magnetic dissipation constant α_B time dependent. The idea here is that, if the evolution of α_B is properly controlled, dissipation will happen only at the places where it is needed and it will be suppressed in all other parts of the simulation volume. The evolution of α_B is controlled by the two parameter S_0 (source term) and C (decay term) where we have chosen α_B^{min} and α_B^{max} as 0.01 and 0.5 respectively. Figure 9 shows the result for varying these two

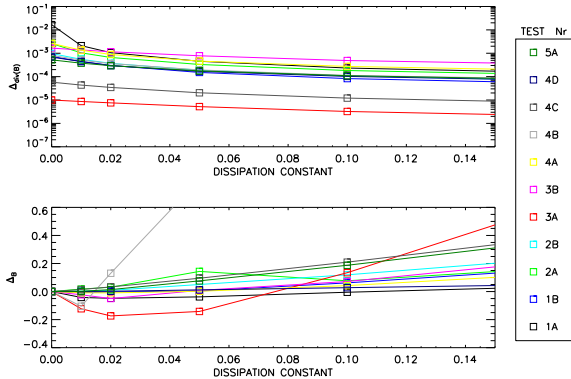


Figure 8. Similar to figure 7 but for different values of the artificial magnetic dissipation constant α_B .

parameters. As before, generally, the larger the dissipation is (e.g. large source term or small decay time) the smaller the noise and the error in $\text{div}(\vec{B})$ becomes. However, as soon as these parameter have values which drive α_B in the shocks to the maximum allowed value, there is marginally no gain in quality, although the values for α_B outside the shocks can still be quite small. Therefore, the time dependent method does not improve the results significantly, as the regions, in which the artificial dissipation constant is suppressed do not significantly contribute to the smearing of sharp features. This is driven in regions, where the artificial magnetic dissipation is anyhow needed to regularize the magnetic field and can not be suppressed there.

3.5 Multi dimensional Tests - Planar Tests

Besides the one dimensional shock tube test described in the previous section, two dimensional (e.g. planar) test problems are a good test-bed to check code performance. Such higher dimensional tests include additional interaction between the evolving components with non-trivial solution. These can be quite complex (with several classes of waves propagating in several directions) such as the Orszang-Tang Vortex or simple (but with strong MHD discontinuities) such as Strong Blast or Fast Rotor.

3.5.1 Fast Rotor

This test problem was introduced by Balsara & Spicer (1999), to study star formation scenarios, in particular the strong torsional Alfvén waves and is also commonly used to validate MHD implementations (for example see Tóth 2000; Londrillo & Del Zanna 2000; Price & Monaghan 2005; Børve et al. 2006). The test consists of a fast rotating dense disk embedded in a low density, static and uniform media, with a initial constant magnetic field along the x -direction (e.g. $B_x = 2.5\pi^{-1/2}$). In the initial conditions, the disk with radius $r = 0.1$, density $\rho = 10$ and pressure $P = 1$ is spinning with an angular velocity $\omega = 20$. It is embedded in a uniform background with $\rho = P = 1$. Again we setup the initial conditions by distributing the particles on a glass like distribution in 3D, using $700 \times 700 \times 5$ particles and periodic boundaries in all directions for the background particles. The disk is created by removing all particles which fall inside the radius of the disk and replacing this space with a denser representation of particles of the same mass.

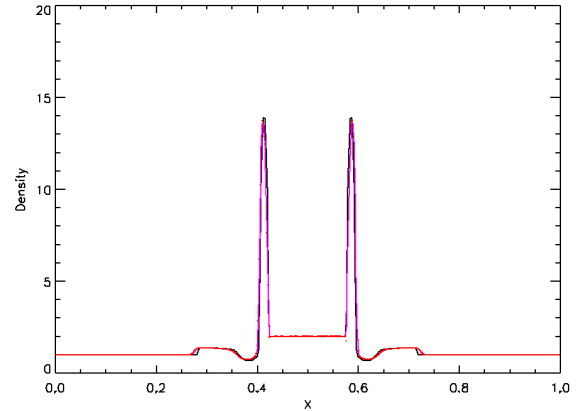


Figure 11. Diagonal ($x = y$) cut through the *Fast Rotor* at $t = 0.1$ showing the density. In black result obtained with ATHENA. The pink line with the red error bars show the GADGET solution using the *standard* MHD implementation. Also here the red error bars reflect the dispersion of the values among individual particles within a slab corresponding to the local smoothing length. In general, the SPH MHD result shows an excellent agreement in all the features (peaks, valleys and edges), however there is a visible over-smoothing at one of the the edges in the GADGET result.

Again we are mimicking realistic conditions as expect in cosmological simulations. As an ideal solution to compare with, we again used the result of a simple, two dimensional ATHENA run with 400×400 cells.

Figure 11 presents a more quantitative comparison. Shown is a diagonal cut through the *Fast Rotor* at $t = 0.1$ showing the density. The different lines show the result obtained with ATHENA (black line) and for the *standard* MHD implementation in GADGET (pink line). The very small, red error bars reflect the RMS of the values held by the individual particles within the 3D slab through the three dimensional simulations corresponding to the local smoothing length. The results show remarkable agreement between the two simulations and also compare well with results quoted in the literature (e.g. Londrillo & Del Zanna 2000)

Note that although we perform our calculations in three dimensions and without a regularization scheme, the implementation produce a result, which has the same quality as other schemes in two dimensions with regularization (e.g. Price & Monaghan 2005; Børve et al. 2006).

3.5.2 Strong Blast

The *Strong Blast* test consists of the explosion of a circular hot gas in a static magnetized medium and is also regularly used for MHD code validation (see for example Londrillo & Del Zanna 2000; Balsara & Spicer 1999). The initial conditions consist of a constant density $\rho = 1$ where a hot disk of radius $r_0 = 0.125$ is embedded, which is hundred times over-pressured, e.g the pressure in the disk is set to $P_d = 100$ whereas the pressure outside the disk is set to $P_o = 1$. Additional there is initially an overall homogeneous magnetic field in the x -direction, with a strength of $B_x = 10$. The system is evolved until time $t = 0.02$ and a outgoing shock wave is visible which, due to the presence of the magnetic field, is not longer spherical but propagates preferentially along the fieldlines. Figure 12 shows the density at the final time, comparing the ATHENA results with the results from the *standard* SPH MHD

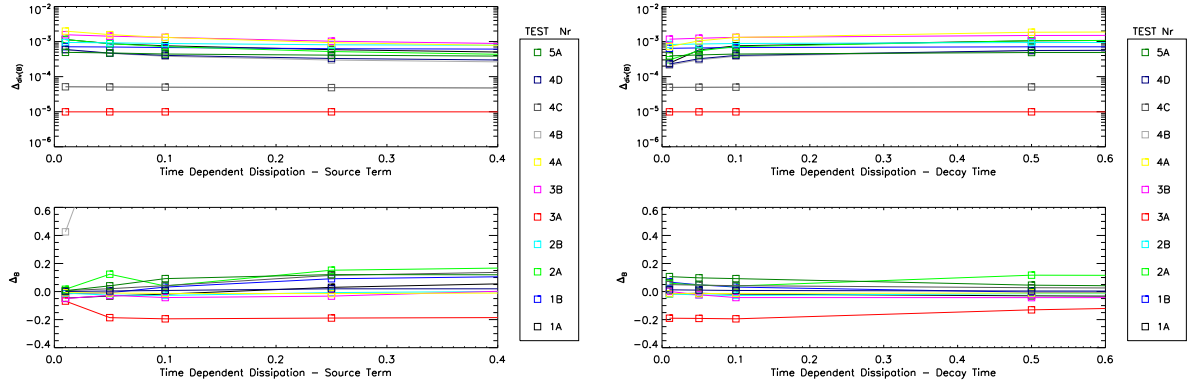


Figure 9. Similar to figure 7 but for different values of the source term S_0 (left panels) and the decay term C (right panel) of the time dependent, artificial magnetic dissipation.

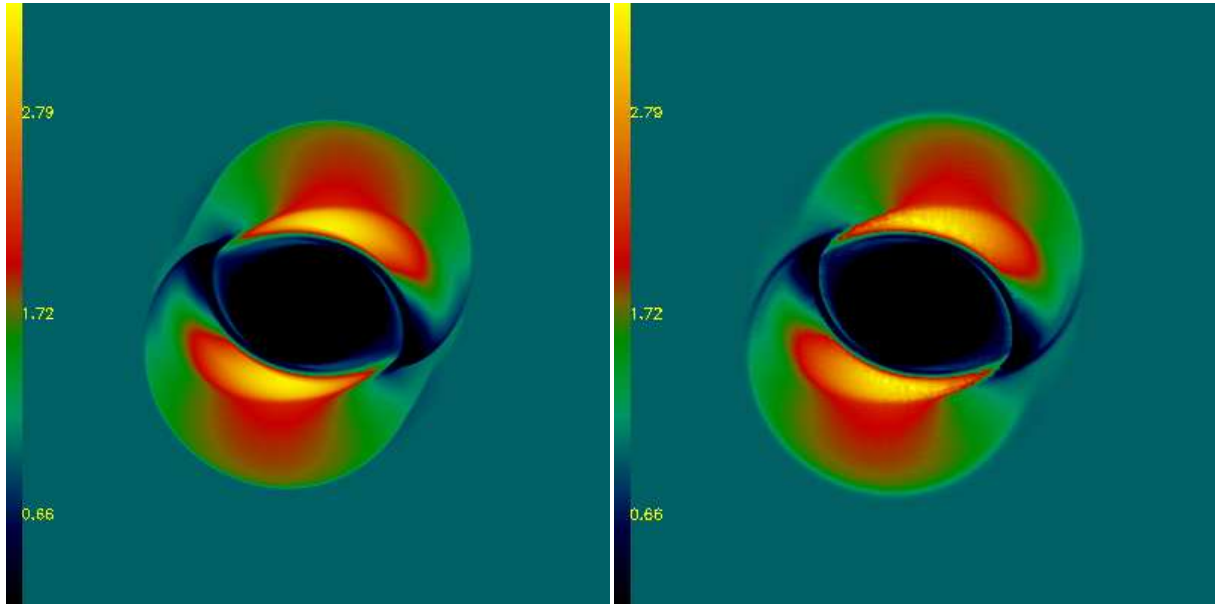


Figure 10. The magnetic pressure ($B^2/2$) in the *Fast Rotor* test at $t = 0.1$. The ATHENA solution of the test problem is shown in the left panel whereas the right panel shows the result obtained with GADGET. All the main features are reproduced in the GADGET run. The shape, positions and amplitudes correspond quite well, although the GADGET run appears slightly more smoothed (see also Figure 11).

implementation in GADGET. Although the setup is a strong blast wave, there is no visible difference of the SPH MHD implementation with the ATHENA results. This is quantitatively confirmed in figure 13 which shows a horizontal cut (at $y = 0.5$) of the density through the *Strong Blast* test, comparing the ATHENA (black line) with the GADGET (pink line with red error bars) results. Besides very small variations there is no significant difference between the two results and all features are well reproduced by the SPH MHD implementation. Note that the error bars of the GADGET results again are almost in all cases smaller than the shown line width.

3.5.3 Orszang-Tang Vortex

This planar test problem, introduced by Orszang & Tang (1979), is well known to study the interaction between several classes of shock waves (at different velocities) and the transition to MHD turbulence. Also this test is commonly used to vali-

date MHD implementations (for example see Dai & Woodward 1994; Picone & Dahlburg 1991; Londrillo & Del Zanna 2000; Price & Monaghan 2005; Børve et al. 2006). The initial conditions for an ideal gas with $\gamma = 5/3$ are constructed within a unit-length domain (e.g. $x = [0, 1], y = [0, 1]$) with periodic boundary conditions. The velocity field is defined by $v_x = -\sin(2\pi y)$ and $v_y = \sin(2\pi x)$. The initial magnetic field is set to be $B_x = B_0 v_x$ and $B_y = B_0 \sin(4\pi x)$. The initial density is $\rho = \gamma P$ and the pressure is set to $P = \gamma B_0^2$. This system is evolved until $t = 0.5$. Figure 14 shows the final result for the magnetic pressure for the ATHENA run (left panel) and the *standard* MHD SPH implementation in GADGET (right panel). Visually the results are quite comparable, however the GADGET results look slightly more smeared, which is the imprint of the underlying SPH method. This impression is confirmed in figure 15, which shows two cuts ($y = 0.3125$ and $y = 0.4277$) through the two simulations. Again, the black line shows the ATHENA result, the pink line with the red error

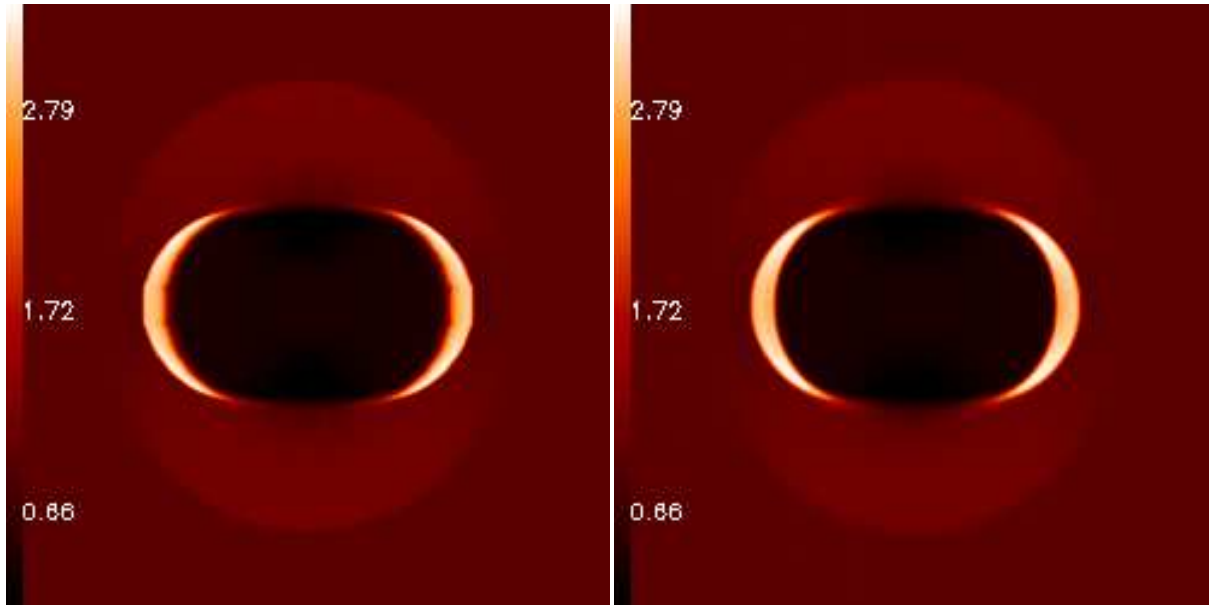


Figure 12. Shown is the resulting density distribution for the *Strong Blast* test at $t = 0.02$. The left panel shows the results obtained with ATHENA, the right panel the results obtained with the *standard* SPH MHD implementation in GADGET. There is no difference between the two results visible (see also figure 13).

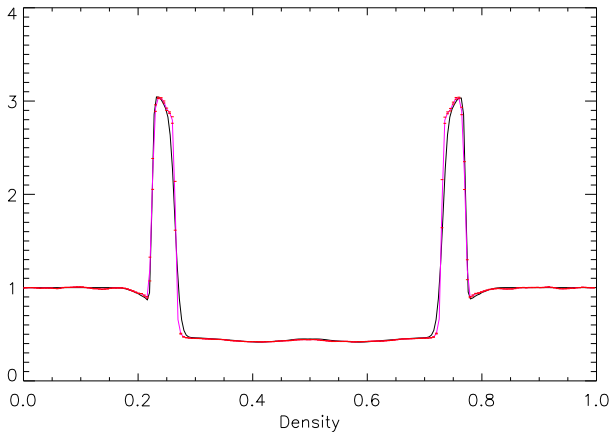


Figure 13. Horizontal cut through the *Strong Blast* test ($x = [0.0; 1.0]$, $y = 0.5$) showing the density. The black line is from the ATHENA simulation, the pink line with the red error bars (see figure 11) reflects the GADGET result. The overall behavior is excellent, with only very small differences between the two solutions.

bars shows the GADGET result. In general there is a reasonable agreement, however the SPH MHD results clearly smooth some of the features. Also the SPH results seems to converge in general slower, the adaptive nature of the SPH MHD implementation allows the central density peak to be resolved whereas in ATHENA is can only be resolved by increasing the resolution. Never-the-less the SPH MHD implementation seems to converge slower when increasing the resolution (see Appendix).

4 COSMOLOGICAL APPLICATION

The cluster used in this work is part of a galaxy cluster sample (Dolag et al., in preparation) extracted from a re-simulation of a

Lagrangian region selected from a cosmological, lower resolution DM-only simulation (Yoshida et al. 2001). This parent simulation has a box-size of 684 Mpc, and assumed a flat Λ CDM cosmology with $\Omega_m = 0.3$ for the matter density parameter, $H_0 = 70$ for the Hubble constant, $f_{bar} = 0.13$ for the baryon fraction and $\sigma_8 = 0.9$ for the normalization of the power spectrum. The cluster has a final mass of $1.5 \times 10^{14} M_\odot$ and was re-simulated at 3 different particle masses for the high resolution region. Using the “Zoomed Initial Conditions” (ZIC) technique (Tormen et al. 1997), these regions were re-simulated with higher mass and force resolution by populating their Lagrangian volumes with a larger number of particles, while appropriately adding additional high-frequency modes drawn from the same power spectrum. To optimize the setup of the initial conditions, the high resolution region was sampled with a 16^3 grid, where only sub-cells are re-sampled at high resolution to allow for quasi arbitrary shapes of the high resolution region. The exact shape of each high-resolution regions was iterated by repeatedly running dark-matter only simulations, until the targeted objects are clean of any lower-resolution boundary particle out to 3-5 virial radii. The initial particle distributions, before adding any Zeldovich displacement, were taken from a relaxed glass configuration (White 1996). The three resolutions used correspond to a mass of the dark matter particles of $1.6 \times 10^9 M_\odot$, $2.5 \times 10^8 M_\odot$ and $1.6 \times 10^8 M_\odot$ for the $1x$, $6x$ and $10x$ simulation. The gravitational softening corresponds to 7, 3.9 and 3.2 kpc respectively. For simplicity we assumed an initially homogeneous magnetic field of 10^{-11} G co-moving as also used in previous work (Dolag et al. 1999, 2002). We also apply the regularization by smoothing the magnetic field in the same way than we did in previous work (Dolag et al. 2004, 2005).

Figure 16 shows a zoom-in from the full cosmological box down to the cluster. The structures in the outer parts get less pronounced due to the decrease in resolution towards the very large scales of the box. Each panel shows (in clockwise order) a zoom-in by a factor of ten. Finally the elongated box in the lower left panel

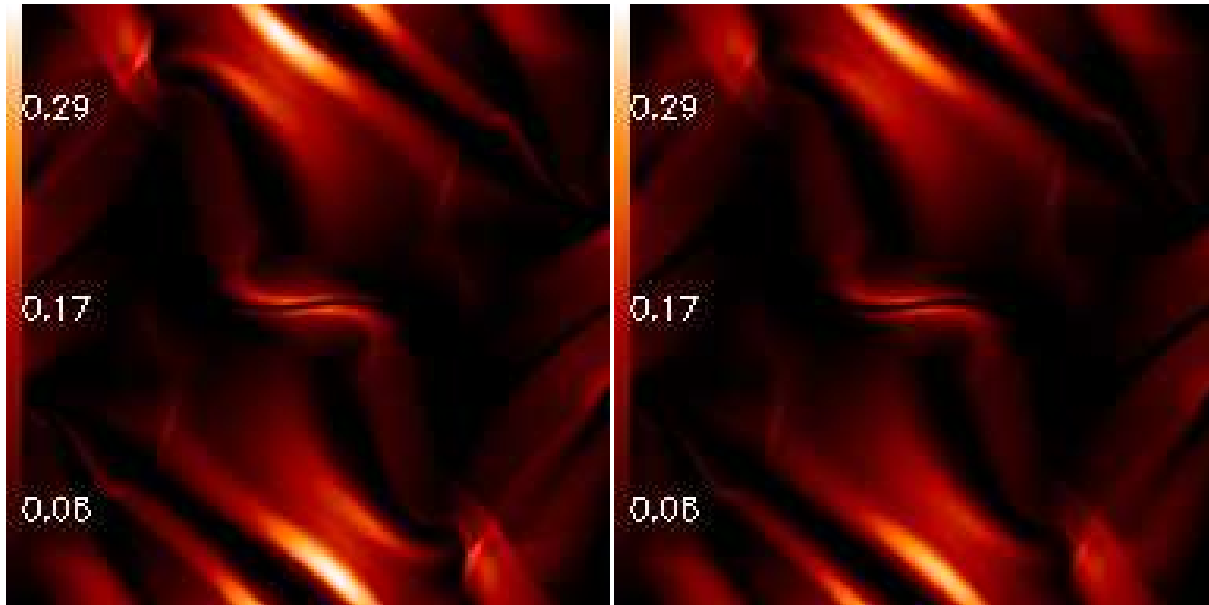


Figure 14. The magnetic pressure $B^2/2$ distribution in the *Orszang-Tang Vortex* at $t = 0.5$. Left panel shows the ATHENA solution and the right panel shows the *standard* SPH MHD implementation in GADGET. Some of the sharp features are smoothed in the SPH MHD implementation but overall the results compares very well (see also figure 15)

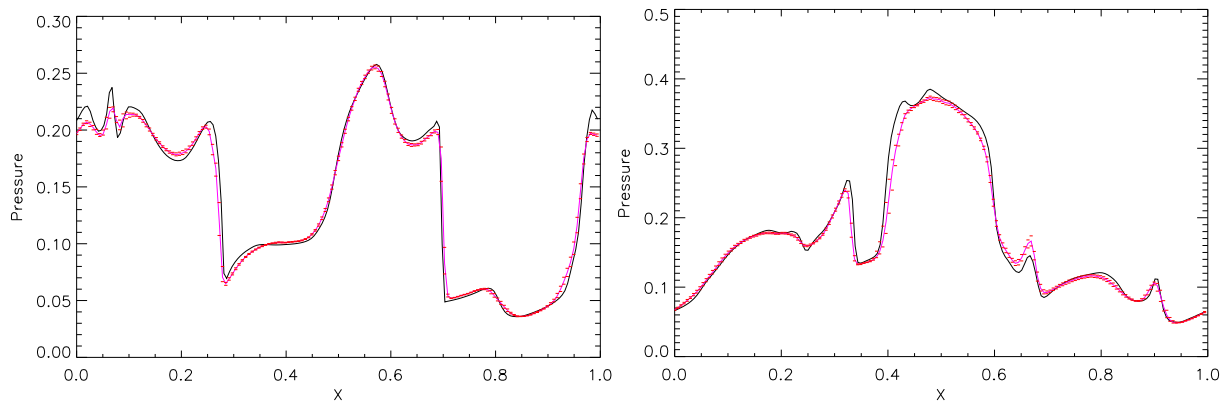


Figure 15. Two $t = 0.5$ cuts through the pressure in the *Orszang-Tang Vortex* at $y = 0.3125$ and at $y = 0.4277$ (left and right panels, respectively). As before, the black line reflect the results obtained with ATHENA and the pink line with the red error bars is obtained with the *standard* SPH MHD implementation in GADGET. The cuts are chosen for comparison with results from the literature, e.g. Børve et al. (2006).

marks the size of the observational frame shown on the left. For comparison we produced a synthetic Faraday Rotation map from the simulation and clipped it to the shape of the actual observations to give an indication of the structures resolved by such simulations. As the initial value of the magnetic field is arbitrary chosen, we used a linear color scale matched to the minimum/maximum values present in the individual maps. The dynamical range of the simulation spawns more than five orders of magnitudes in spatial dimension, and the size of the underlying box is 6 and 5 times larger than the AMR simulations presented in Dubois & Teyssier (2008) and Brügger et al. (2005), respectively. Still the resolution of the underlying dark matter distribution is, respectively, 2 and 5 times better than these AMR simulations and the cluster is resolved with more than one million dark matter particles within the virial radius at the $10x$ resolution. To perform the simulation, the $10x$ resolution run needed ≈ 730 CPUh on an AMD Opteron cluster. This again

is demonstrating the advantages of the underlying SPH scheme in making large, cosmological zoomed simulations possible.

In figure 17, the radial magnetic field profiles are shown for the three resolutions comparing the results obtained with the normal configuration for cosmological simulations with results where we just used the *Euler Potential* to follow the evolution of the magnetic field ignoring back reactions. As already noted in earlier work (Dolag et al. 2002), the left panel shows the dependence of the amplification of magnetic fields with resolution. In addition, the solution obtained with the *Euler Potential* agrees nicely with the *standard* runs in the outer part of the profiles. In the central parts, the *standard* simulation falls below the solution obtained using the *Euler Potential*. This is easy to understand, because the *Euler Potential* are free from any numerical magnetic dissipation. Additional the magnetic field is strongest in the cluster core and therefore, including the magnetic force in the normal runs will lead to a sup-

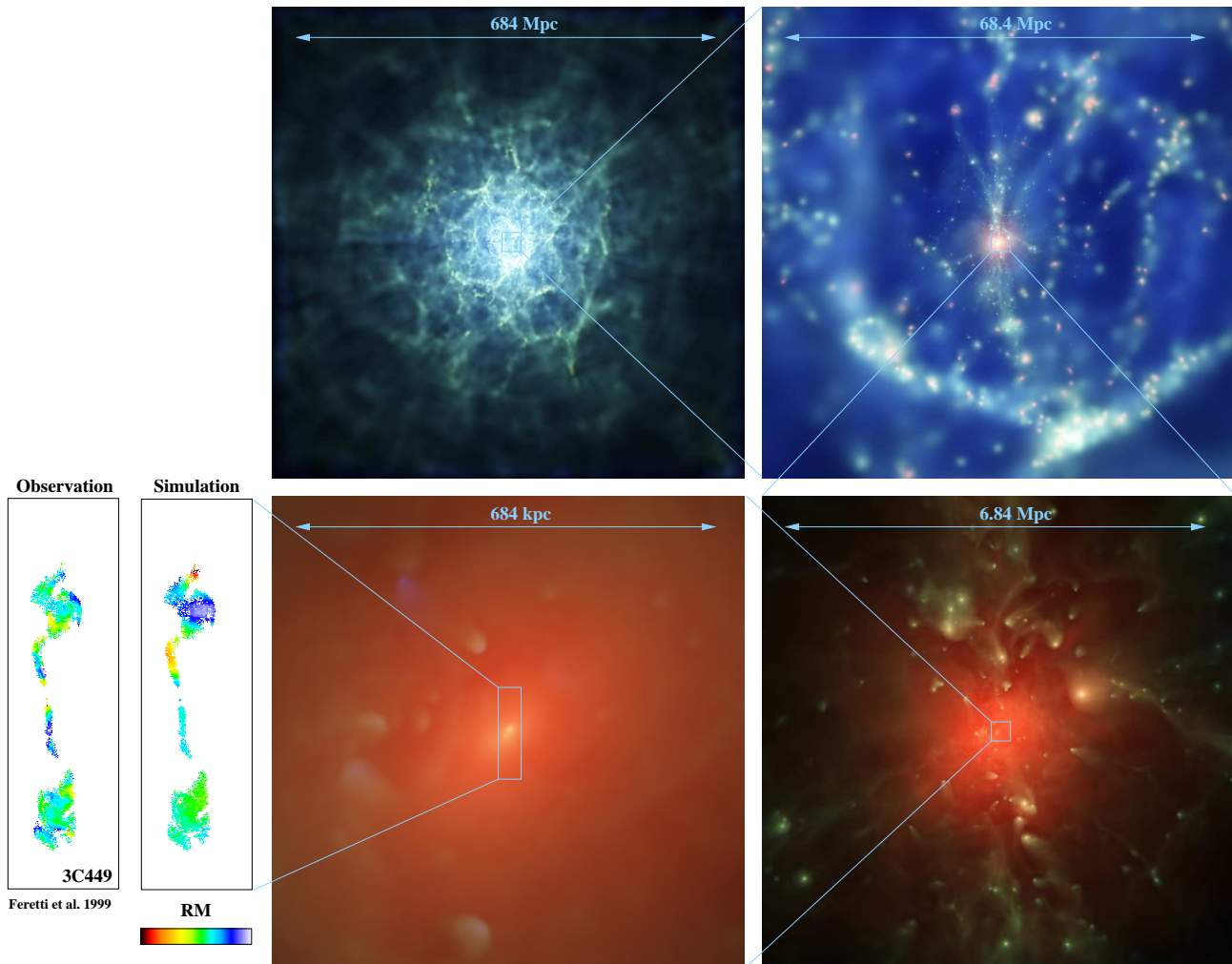


Figure 16. Zoom into the cluster simulated within the cosmological box. Clockwise, each panel displays a factor 10 increase in imaging magnification, starting from the full box (684 Mpc) down to the cluster center (680 kpc). On the very large scale, the density of the dark matter particles are shown, whereas in the high resolution region the temperature of the gas is rendered to emphasize the presence and dynamics of the substructure. The last zoom extracts a region of the same size of an observed radio jet (3C449) with measured rotation measure (Feretti et al. 1999). Both, the simulated and the observed map are displayed using a linear color-scale based on the minimum and maximum values in the maps. The synthetic RM map is clipped to the shape of the observations. Clearly, the simulations are still lacking in resolution, however they do come quite close.

pression of the amplification. In general the comparison of the two methods demonstrate that the amplification of the magnetic field in the *standard* implementation is not significantly influenced by the non-zero $\text{div}(\vec{B})$. In addition, although the absolute value of the amplification is not converged with resolution, the shape of the predicted magnetic field profile appears to be converged. This is shown in the right panel of figure 17, where the profiles are normalized artificial at large radii to demonstrate the self similar shapes. Note that this convergence, as usual for all hydro dynamical quantities, is only reached at radii significant larger than the size of the gravitational softening, indicated as dashed lines for the lowest (e.g. $1x$) and highest (e.g. $10x$) resolution runs.

The situation changes when using artificial magnetic dissipation, as shown in figure (18). The left panel shows the magnetic field profiles for several values of α_B compared with the profiles for the *standard* run and that using *Euler Potentials*. Clearly a normal value for artificial magnetic dissipation leads to a large dissipation of magnetic field over the simulation time (e.g. close to the Hubble

time). The right panels show the profiles artificially normalized at large radius. Clearly the self similarity of the profiles is lost. Therefore it looks like that the use of artificial dissipation as a regularization scheme is not a good choice for cosmological simulations. Additional it points out that physical dissipation might play an important role in determining the shape of the magnetic field profile in galaxy clusters.

5 CONCLUSIONS

We presented the implementation of MHD in the cosmological, SPH code GADGET. We performed various test problems and discussed several instability correction and regularization schemes. We also demonstrated the application to cosmological simulations, the role of resolution and the role the regularization schemes play in cosmological simulations.

Our main findings are:

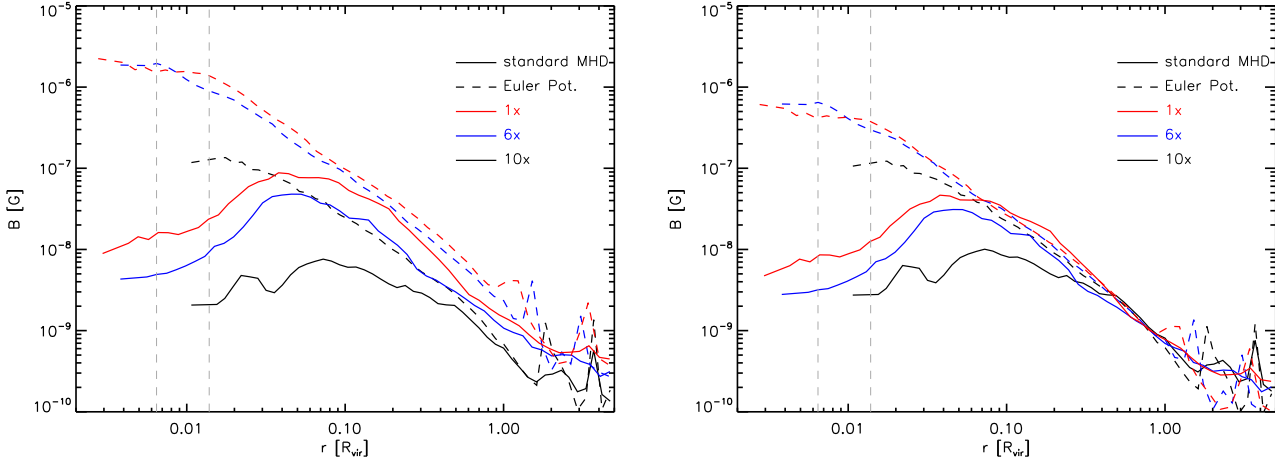


Figure 17. The magnetic field profiles for a resolution study of our cluster. Solid lines are obtained with the standard implementation, dashed lines are for using Euler potentials. The different line colors indicating different resolution. Right panel shows the same but normalizing all the profiles in the outer part of the cluster.

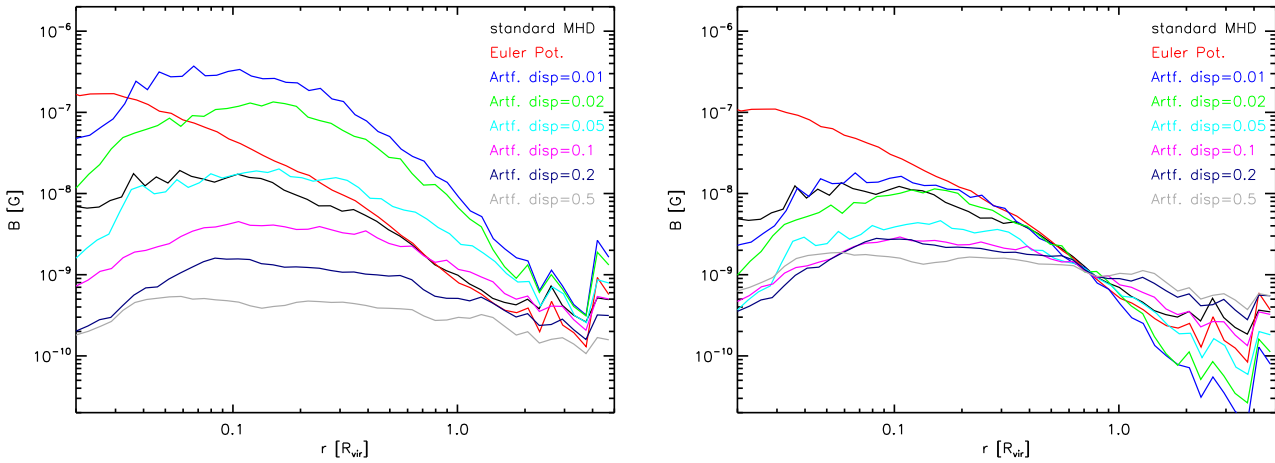


Figure 18. The magnetic field profiles obtained for the galaxy cluster using different regularization methods. In Addition the results for using the *Euler Potentials* are shown. Right panel shows the same with profiles normalized in the outer part of the cluster.

- The combination of many improvements in the SPH implementation, like the correction terms for the variable smoothing length (Springel & Hernquist 2002) as well as the usage of the signal velocity in the artificial viscosity (Monaghan 1997) together with its generalization to the MHD case (Price & Monaghan 2004a) improve the handling of magnetic fields in SPH significantly.
- Correcting the instability by explicitly subtracting the contribution of a numerical non-zero divergence of the magnetic field to the Lorenz force from the Maxwell tensor as suggested by Børve et al. (2001) seems to perform well. Specifically in three dimensional setups it seem to work much better than other suggestions in the literature.
- The SPH MHD implementation performs very well on simple shock tube tests as well as on planar test problems. We performed all test in a fully three-dimensional setup and find excellent agreement of the results obtained with the SPH MHD implementation

- compared to the results obtained with ATHENA in one or two dimensions.
- With a convergence study we demonstrate that the SPH MHD results when increasing the resolution are converging to the true solution, especially in the sharp features. However, in some regions it seems that small but systematic differences converge only very slowly to the correct solution, which most likely is related to biases in the underlying density estimation.
 - Regularization schemes help to further suppresses noise and $\text{div}(\vec{B})$ errors in the test simulations, however one has to carefully select the numerical parameters to avoid too strong smoothing of sharp features. Performing a full set of individual shock tube tests allows one to tune the numerical schemes and to determine optimal values.
 - The SPH MHD implementation allows us to perform challenging cosmological simulations, covering a large dynamical range in length-scales. For galaxy clusters the shape of the predicted magnetic profiles is, (with the exception of the central part

of clusters) converged in resolution and in good agreement with previous studies. Also the structures obtained in synthetic Faraday Rotation maps are in good agreement with previous findings and compare well with observations.

The results obtained with artificial dissipation in cosmological simulations indicate that physical dissipation could play a crucial role in determining the exact shape of the predicted, magnetic field profiles in galaxy clusters. Future work, especially when including more physical processes at work in galaxy cluster – as can be done easily with our SPH MHD implementation – will reveal an interesting interplay between dynamics of the cluster atmosphere and amplification of magnetic fields. Thus having the potential to shed light on many, currently unknown aspects of cluster magnetic fields, their structure and their evolution.

ACKNOWLEDGEMENTS

KD acknowledges the financial support by the “HPC-Europa Transnational Access program” and the hospitality of CINECA and “Istituto di Radioastronomia” (IRA) in bologna, where part of the work was carried out. FAS acknowledges the support of the European Union’s ALFA-II programme, through LENAC, the Latin American European Network for Astrophysics and Cosmology. We want to thank Stuart Sim for carefully reading and improving the manuscript. We also want to thank James M. Stone for making ATHENA – which we used for obtaining our reference solutions – publicly available as well as Romain Teyssier for sending us the results for the Orszang-Tang Vortex test obtained with RAMSES. We further thank Daniel Price for many enlightening discussions and Volker Springel to always granting access to the developer version of GADGET. We also want to thank Luigina Feretti for providing the RM map of 3C449.

REFERENCES

- Balsara D. S., 1995, *Journal of Computational Physics*, 121, 357
 Balsara D. S., Spicer D. D., 1999, *Journal of Computational Physics*, 149, 270
 Børve S., Omang M., Trulsen J., 2001, *ApJ*, 561, 82
 Børve S., Omang M., Trulsen J., 2004, *ApJS*, 153, 447
 Børve S., Omang M., Trulsen J., 2006, *ApJ*, 652, 1306
 Brio M., Wu C. C., 1988, *Journal of Computational Physics*, 75, 500
 Brüggem M., Ruszkowski M., Simionescu A., Hoeft M., Dalla Vecchia C., 2005, *ApJ*, 631, L21
 Carilli C. L., Taylor G. B., 2002, *ARAA*, 40, 319
 Dai W., Woodward P. R., 1994, *Journal of Computational Physics*, 115, 485
 Del Pra M., 2003, *Laurea Thesis*
 Dolag K., 2000, in *Constructing the Universe with Clusters of Galaxies Properties of Simulated Magnetized Galaxy Clusters*
 Dolag K., Bartelmann M., Lesch H., 1999, *A&A*, 348, 351
 Dolag K., Bartelmann M., Lesch H., 2002, *A&A*, 387, 383
 Dolag K., Grasso D., Springel V., Tkachev I., 2004, *Soviet Journal of Experimental and Theoretical Physics Letters*, 79, 583
 Dolag K., Grasso D., Springel V., Tkachev I., 2005, *Journal of Cosmology and Astro-Particle Physics*, 1, 9
 Dolag K., Jubelgas M., Springel V., Borgani S., Rasia E., 2004, *ApJ*, 606, L97
 Dubois Y., Teyssier R., 2008, *A&A*, 482, L13
 Enßlin T. A., Pfrommer C., Springel V., Jubelgas M., 2007, *A&A*, 473, 41
 Feretti L., Perley R., Giovannini G., Andernach H., 1999, *A&A*, 341, 29
 Ferrari C., Govoni F., Schindler S., Bykov A. M., Rephaeli Y., 2008, *Space Science Reviews*, 134, 93
 Gingold R. A., Monaghan J. J., 1977, *MNRAS*, 181, 375
 Govoni F., Feretti L., 2004, *International Journal of Modern Physics D*, 13, 1549
 Jubelgas M., Springel V., Dolag K., 2004, *MNRAS*, 351, 423
 Kulsrud R. M., Cen R., Ostriker J. P., Ryu D., 1997, *ApJ*, 480, 481
 Li S., Li H., Cen R., 2008, *ApJS*, 174, 1
 Londrillo P., Del Zanna L., 2000, *ApJ*, 530, 508
 Lucy L. B., 1977, *AJ*, 82, 1013
 Monaghan J. J., 1997, *Journal of Computational Physics*, 136, 298
 Monaghan J. J., 2000, *J. Comput. Phys.*, 159, 290
 Monaghan J. J., Lattanzio J. C., 1985, *A&A*, 149, 135
 Morris J. P., Monaghan J. J., 1997, *Journal of Computational Physics*, 136, 41
 Omang M., Børve S., Trulsen J., 2006, *Journal of Computational Physics*, 213, 391
 Orszang S. A., Tang C. M., 1979, *Journal of Fluid Mechanics*, 90, 128
 Pfrommer C., Enßlin T. A., Springel V., Jubelgas M., Dolag K., 2007, *MNRAS*, 378, 385
 Phillips G. J., Monaghan J. J., 1985, *MNRAS*, 216, 883
 Picone J. M., Dahlburg R. B., 1991, *Physics of Fluids B*, 3, 29
 Price D. J., Monaghan J. J., 2004a, *MNRAS*, 348, 123
 Price D. J., Monaghan J. J., 2004b, *MNRAS*, 348, 139
 Price D. J., Monaghan J. J., 2005, *MNRAS*, 364, 384
 Rordorf C., Grasso D., Dolag K., 2004, *Astroparticle Physics*, 22, 167
 Rosswog S., Price D., 2007, *MNRAS*, 379, 915
 Ryu D., Jones T. W., 1995, *ApJ*, 442, 228
 Ryu D., Kang H., Biermann P. L., 1998, *A&A*, 335, 19
 Ryu D., Kang H., Cho J., Das S., 2008, *Science*, 320, 909
 Sigl G., Miniati F., Enßlin T. A., 2004, *Phys. Rev. D*, 70, 043007
 Sijacki D., Springel V., 2006, *MNRAS*, 371, 1025
 Springel V., 2005, *MNRAS*, 364, 1105
 Springel V., Hernquist L., 2002, *MNRAS*, 333, 649
 Springel V., Hernquist L., 2003, *MNRAS*, 339, 289
 Springel V., White M., Hernquist L., 2001, *ApJ*, 549, 681
 Steinmetz M., 1996, in *IAU Symp. 171: New Light on Galaxy Evolution Mergers and Formation of Disk Galaxies in Hierarchically Clustering Universes*. p. 259
 Stone J. M., Gardiner T. A., Teuben P., Hawley J. F., Simon J. B., 2008, *ArXiv e-prints*, 804
 Teyssier R., 2002, *A&A*, 385, 337
 Tormen G., Bouchet F. R., White S. D. M., 1997, *MNRAS*, 286, 865
 Tornatore L., Borgani S., Dolag K., Matteucci F., 2007, *MNRAS*, 382, 1050
 Tornatore L., Borgani S., Matteucci F., Recchi S., Tozzi P., 2004, *MNRAS*, 349, L19
 Tóth G., 2000, *Journal of Computational Physics*, 161, 605
 White S. D. M., 1996, in *Schaeffer R., Silk J., Spiro M., Zinn-Justin J., eds, Cosmology and Large Scale Structure Formation and Evolution of Galaxies*. pp 349–+
 Yoshida N., Sheth R. K., Diaferio A., 2001, *MNRAS*, 328, 669

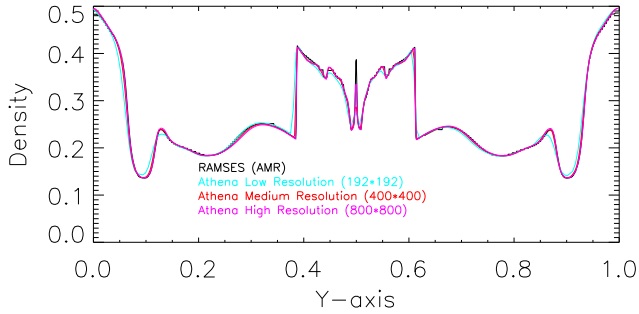


Figure A1. A cut through the density for the Orszang-Tang Vortex test (see Figure 13/14). Shown in black is the result obtained with Ramses, compared to the results obtained with Athena using 3 different resolutions.

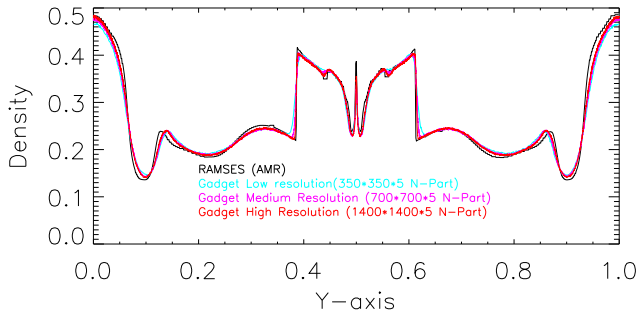


Figure A2. Same than figure (A1), but showing the results obtained with the *standard* SPH-MHD implementation at two different resolutions compared to the results obtained with Ramses.

APPENDIX A: CONVERGENCE

Numerical experiments are normally restricted by the resolution once can technically (in terms of computing/memory requirements) achieve. Therefore tests as presented in section 3 are usually at nominal better resolution than can be obtained in relevant (in this case cosmological) simulations. Never-the-less an interesting question is, how good do the numerical methods used converge if once further increase the resolution strongly? Figure A1 and A2 show this for Athena and the *standard* SPH-MHD implementation respectively. We repeated the Orszang-Tang Vortex test problem with Athena on a 192^2 , 400^2 and 800^2 grid. Figure A1 shows a cut through the density of the Orszang-Tang Vortex, comparing with the result obtained with the AMR code Ramses (Teyssier 2002). Clearly, the results obtained with Athena when increasing the resolution approaches the results obtained with Ramses. Figure A2 shows the same for setups with $350^2 \times 5$, $700^2 \times 5$ and $1400^2 \times 5$ particles. The SPH-MHD implementation also converges towards the Ramses results with increasing resolution. But although the central feature is better resolved in the SPH-MHD implementation than in the Athena run with comparable resolution, some other features can be seen to converge slower in the SPH-MHD implementation when increasing the resolution. Specifically, in some very smoothed features it looks like that there are small but systematic differences between the SPH and the true solution. Here the SPH results seems to converge only extremely slow (if at all). This is most likely related to systematics in the underlying density estimation.